Surface tension effects between two immiscible Stokes fluids: a computational study using unfitted hybrid high-order methods and a level-set scheme

Stefano Piccardo & Alexandre Ern

Surface tension effects between two immiscible Stokes fluids: a computational study using unfitted hybrid high-order methods and a level-set scheme

STEFANO PICCARDO [1]
ALEXANDRE ERN [2]

[1] CERMICS, Ecole des Ponts, 77455 Marne-la-Vallée 2, France; Inria, 2 rue Simone Iff, 75589 Paris, France; LaCàN, ETS de Ingenieros de Caminos, Canales y Puertos, Universitat Politècnica de Catalunya, 08034 Barcelona, Spain
E-mail address: stefano.piccardo@upc.edu
[2] CERMICS, Ecole des Ponts, 77455 Marne-la-Vallée 2, France; Inria, 2 rue Simone Iff, 75589 Paris, France
E-mail address: alexandre.ern@enpc.fr.

Abstract. We develop an unfitted Hybrid High-Order (HHO) method coupled with a level-set scheme to solve numerically the flow of two immiscible Stokes fluids separated by an unknown interface where surface tension effects are present. The interface can cut through the mesh cells and a cell-agglomeration procedure is used to prevent possible ill-conditioning caused by small cut cells. The first computational study concerns the equilibrium between pure shear flow at infinity and surface tension, leading to an interface with elliptic shape. In particular, the dependence of the capillarity number on the Taylor deformation parameter and the viscosity ratio of both fluids is investigated. The second computational study covers evolving interfaces and illustrates how an initial interface progressively relaxes toward equilibrium.

2020 Mathematics Subject Classification. 65N30, 65N22, 65N85, 76D45.
Keywords. Hybrid discretization methods, Unfitted meshes, Stokes flows, Immiscible fluids, Surface tension.

1. Introduction

In this work, we study the equilibrium of two immiscible, incompressible Stokes fluids separated by a single interface where surface tension effects are present [8, 34, 38]. The interface, whose shape is part of the unknowns of the problem, splits the computational domain into two subdomains, and each subdomain is occupied by a fluid governed by the steady, incompressible Stokes equations. At the interface, the fluid velocities are continuous, the normal velocity vanishes, and the jump of the normal component of the total stress is proportional to the curvature of the interface (Laplace's law). The present model, albeit simplified, has relevant applications in microfluidics, where the surface tension dominates the emulsion process [20]. Over the last decades, microfluidics has gained growing importance in domains such as medicine, biology and chemistry [1, 28].

Solving the above problem computationally is quite challenging because the shape of the interface is unknown. A natural approach is to resort to a fixed-point iterative procedure where each iteration is decomposed into two substeps. In the first substep, the shape of the interface is kept fixed, and a so-called Stokes interface problem is solved, whereby the interface conditions enforce only the continuity of the fluid velocities and the jump of the normal stresses, but the normal velocity at the interface may be nonzero. In the second substep, the flow field of both fluids is kept fixed, and the interface is evolved using a level-set scheme. In this context, using an unfitted method in the first substep is quite attractive since it allows one to use the same background mesh for all the iterations of the fixed-point

procedure. The main goal of the present work is to develop an unfitted hybrid high-order (HHO) method coupled with a level-set scheme to solve the above interface problem.

HHO methods on fitted meshes have been introduced in [16] for locking-free linear elasticity and in [17] for linear diffusion, and they are closely related to hybridizable discontinuous Galerkin, non-conforming virtual element, and weak Galerkin methods [14]. When applied to incompressible Stokes flows, the HHO method employs hybrid unknowns (face- and cell-based) for the velocity and only cell-based unknowns for the pressure [3, 18]. The method is inf-sup stable, locally conservative, supports polytopal meshes, and is computationally efficient owing to its compact stencil and to the possibility of a local elimination of the cell velocity unknowns by a static condensation procedure. Unfitted HHO methods for elliptic interface problems with known interface have been derived in [9, 11] using two key ideas. First, one doubles the (cell and face) unknowns in every cut cell without introducing any face unknown at the interface, and the jump conditions at the interface are enforced by means of a consistent penalty technique in the spirit of [25]. Second, a local cell-agglomeration procedure is used to counter the adverse effects of ill-cut cells (see also [30, 36] for cell-agglomeration procedures in the discontinuous Galerkin context). These ideas were extended in [10] to the Stokes interface problem, still assuming a known interface.

In the paper, we extend [9] in three directions, while using the same cell-agglomeration procedure. First, we consider surface tension effects. This, in particular, requires to approximate the curvature of the interface at all the integration points along the interface. Second, the quadratures in the cut cells used in [10] are based on a subpartition of the cut cell using affine triangles, whereas we introduce here a more effective approach based on an isoparametric description of the interface. Third, this work devises, for the first time, a coupling between the unfitted HHO method and a level-set scheme to track the interface. While HHO methods offer various assets (high-order, support of polyhedral meshes, computational efficiency, local conservation), we observe that several other methods are available in the literature to approximate the Stokes interface problem; see, e.g., [5, 12, 13, 26, 29, 35] for finite element and [2, 27, 36] for discontinuous Galerkin discretizations. We also notice that considering the Stokes equations is reasonable in view of microfluidics applications. One can also consider the Navier–Stokes equations, for which HHO methods on fitted meshes were constructed, e.g., in [7].

Our computational study covers two main test cases, which are both two-dimensional. The first one is devoted to the equilibrium between a pure shear flow (enforced far away from the interface, no body forces) and surface tension effects. In this case, the equilibrium interface is known to be an ellipse (the area of the ellipse still remains a free parameter in the problem), and, fixing the viscosity ratio of both fluids, the ellipse eccentricity depends upon the ratio of the prescribed shear to surface tension (also called capillary number) [15, 21, 38]. When the capillary number is zero (no prescribed shear, flow at rest), the ellipse eccentricity is zero, that is, the ellipse becomes a circle. In the present work, we investigate numerically the dependence of the ellipse eccentricity on the capillary number. A linear relationship is expected, as predicted theoretically in [38]. Our contribution is to quantify the slope of this relationship as a function of the viscosity ratio of both fluids. Since the shape of the equilibrium interface is known in this first test case, we do not need to invoke the above fixed-point iterative procedure. In practice, we pose the Stokes interface problem on a finite computational box surrounding the elliptic equilibrium interface, and we verify numerically that the expected equilibrium is fairly well attained even on moderately large computational domains.

The second test case involves the more challenging setting where the boundary conditions (and possibly the body forces) are more complex, so that the equilibrium interface has no longer an elliptic shape. The shape of the interface then becomes an unknown of the problem that is determined by the above fixed-point iterative procedure. Notice that we do not perform here a convergence analysis of this fixed-point procedure; this is a difficult problem left for future work. We merely observe that the procedure is consistent since, assuming convergence, the interface becomes stationary so that the normal flow velocity at the interface is zero. The position of the interface is classically described

by means of a level-set function. To transport the level-set function, possible approaches are finite volume [32, 33, 37], discontinuous Galerkin [6], and continuous finite element methods [22]; herein, we use the latter. One important challenge encountered in flow problems dominated by surface tension resides in the approximation of the curvature at the interface. To reduce oscillations, possible strategies are the use of coarser meshes for the level-set discretization (but possibly increasing the so-called mass loss effects), or the smoothing of the normal and the curvature by means of a global projection in the whole computational domain [33] (but possibly affecting the approximation quality). We propose here a somewhat alternative strategy, where we construct a parametric interface of arbitrary order from the level-set function, and then we project the normal and the curvature derived from the level-set function locally on this parametric interface.

The paper is organized as follows. Section 2 is devoted to the presentation of the model problem. Section 3 describes the unfitted HHO solver for the Stokes interface problem. Section 4 presents the results when the shape of the interface is elliptic, whereas Sections 5 and 6 deal respectively with the methodology and the results when the shape of the interface is unknown. As mentioned above, this work is restricted to the two-dimensional setting. The main obstacle to a three-dimensional extension is the handling of the mesh cells cut by the interface, the representation of the latter within the cut cells, and the cell-agglomeration procedure. While these steps are feasible, they represent at the time of writing a further, non-trivial implementation effort.

2. Model problem

Let $\Omega_i \subset \mathbb{R}^d$, $d = 2$, be two domains (connected, bounded, open Lipschitz sets) with Ω_i occupied by the fluid indexed by $i \in \{1, 2\}$. The interface is $\Gamma := \partial\Omega_1 \cap \partial\Omega_2$, and the computational domain Ω is $\overline{\Omega} := \overline{\Omega}_1 \cup \overline{\Omega}_2$. For simplicity, we assume that Ω is a polygon/polyhedron so that it can be meshed exactly. Moreover, we assume that the interface Γ is closed and does not touch the boundary $\partial\Omega$ of Ω. By convention, the index 1 refers to the interior subdomain Ω_1 such that $\partial\Omega_1 = \Gamma$, and the index 2 refers to the exterior subdomain Ω_2 such that $\partial\Omega_2 = \partial\Omega \cup \Gamma$, see Figure 2.1. The interface Γ is assumed to be orientable, and such that a unit normal, $\boldsymbol{n}_\Gamma$, can be defined everywhere on Γ. Since $d = 2$, the interface Γ is a one-dimensional manifold. By convention, $\boldsymbol{n}_\Gamma$ points from Ω_1 to Ω_2, i.e., Γ is oriented counter-clockwise.
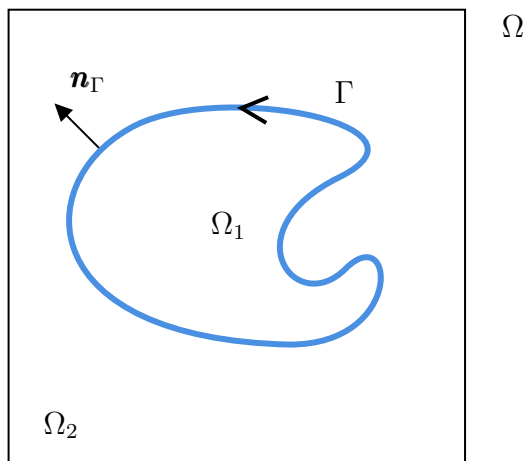
FIGURE 2.1. Computational domain Ω, subdomains Ω_i, $i \in \{1, 2\}$, interface Γ, and unit normal $\boldsymbol{n}_\Gamma$.

We consider two immiscible, incompressible fluids separated by the interface Γ. In the so-called *Stokes interface problem*, the interface Γ is prescribed, and we seek the velocity and pressure fields $(\boldsymbol{u}_i, p_i) \in H^1(\Omega_i; \mathbb{R}^d) \times L^2(\Omega_i)$, $i \in \{1, 2\}$, such that

$$-\nabla \cdot \boldsymbol{\sigma}_i = \boldsymbol{f}_i \quad \text{in } \Omega_i, \quad i \in \{1, 2\}, \tag{2.1a}$$

$$\nabla \cdot \boldsymbol{u}_i = 0 \quad \text{in } \Omega_i, \quad i \in \{1, 2\}, \tag{2.1b}$$

$$\boldsymbol{u}_2 = \boldsymbol{g} \quad \text{on } \partial\Omega, \tag{2.1c}$$

$$[\![\boldsymbol{u}]\!] = \boldsymbol{0}, \quad [\![\boldsymbol{\sigma}]\!]\boldsymbol{n}_\Gamma = \boldsymbol{g}_N \quad \text{on } \Gamma, \tag{2.1d}$$

where the total stress tensor for each fluid is

$$\boldsymbol{\sigma}_i := 2\mu_i \nabla^{\mathrm{s}}\boldsymbol{u}_i - p_i\mathbb{l}, \quad \nabla^{\mathrm{s}}\boldsymbol{u}_i := \frac{1}{2}(\nabla\boldsymbol{u}_i + \nabla\boldsymbol{u}_i^{\mathrm{T}}), \tag{2.2}$$

μ_i is the viscosity of the fluid i and $\mathbb{l}$ the identity tensor. Moreover, $[\![v]\!] := (v|_{\Omega_1})|_\Gamma - (v|_{\Omega_2})|_\Gamma$ denotes the jump of a piecewise smooth function v across Γ (the jump is defined component-wise for a vector- or tensor-valued field, and its sign is consistent with the orientation of the unit normal $\boldsymbol{n}_\Gamma$). To model the surface tension according to Laplace's law, we set

$$\boldsymbol{g}_N = \gamma H_\Gamma \boldsymbol{n}_\Gamma, \tag{2.3}$$

where γ is the surface tension and H_Γ the curvature on the interface.

The problem data are the body forces $\boldsymbol{f}_i \in L^2(\Omega_i; \mathbb{R}^d)$, $i \in \{1, 2\}$, and the Dirichlet boundary condition $\boldsymbol{g} \in H^{\frac{1}{2}}(\partial\Omega; \mathbb{R}^d)$. The Stokes interface problem is well-posed if

$$\int_{\partial\Omega} \boldsymbol{g} \cdot \boldsymbol{n}_\Omega = 0 \tag{2.4}$$

(implied by the incompressibility condition), with $\boldsymbol{n}_\Omega$ the unit outward normal to Ω and if one requires $\sum_{i \in \{1,2\}} \int_{\Omega_i} p_i = 0$, thereby fixing the global additive constant on the pressure.

In the more general *interface equilibrium problem*, the interface Γ is part of the unknowns of the problem. In this setting, the Stokes interface problem is completed by requiring that the normal velocity at the interface is zero, and this condition essentially prescribes the shape of the interface. Thus, in the interface equilibrium problem, we seek the velocity and pressure fields $(\boldsymbol{u}_i, p_i) \in H^1(\Omega_i; \mathbb{R}^d) \times L^2(\Omega_i)$, $i \in \{1, 2\}$, and the interface Γ such that

$$(2.1) \text{ holds true} \quad + \quad \boldsymbol{u} \cdot \boldsymbol{n}_\Gamma = 0 \text{ on } \Gamma, \tag{2.5}$$

where $\boldsymbol{u} := \boldsymbol{u}_1 = \boldsymbol{u}_2$ on Γ by (2.1d). Notice that equilibrium requires a zero normal velocity at the interface, whereas no conditions are imposed on the tangential velocity since it does not affect the shape of the interface.

It is convenient to describe the interface Γ as being the zero level-set of a function $\phi : \Omega \to \mathbb{R}$, i.e.,

$$\Gamma := \{\boldsymbol{x} \in \Omega : \phi(\boldsymbol{x}) = 0\}, \tag{2.6}$$

and by convention, we assume that $\Omega_1 = \{\boldsymbol{x} \in \Omega : \phi(\boldsymbol{x}) < 0\}$ and $\Omega_2 = \{\boldsymbol{x} \in \Omega : \phi(\boldsymbol{x}) > 0\}$. Assuming that ϕ is of class $\mathcal{C}^2$ in a neighborhood of Γ, we set

$$\boldsymbol{n}_\phi = \frac{\nabla\phi}{\|\nabla\phi\|_{\ell^2}}, \qquad H_\phi = -\nabla \cdot \boldsymbol{n}_\phi = -\frac{\Delta\phi}{\|\nabla\phi\|_{\ell^2}} + \frac{1}{\|\nabla\phi\|_{\ell^2}^3} D^2\phi(\nabla\phi, \nabla\phi), \tag{2.7}$$

where $\|\cdot\|_{\ell^2}$ denotes the Euclidean norm in $\mathbb{R}^d$ and $D^2\phi(\cdot, \cdot)$ is the quadratic form associated with the Hessian of ϕ, and then obtain the unit normal and the curvature of Γ by setting

$$\boldsymbol{n}_\Gamma := \boldsymbol{n}_\phi|_\Gamma, \qquad H_\Gamma := H_\phi|_\Gamma. \tag{2.8}$$

Notice that the curvature is negative everywhere on Γ if the set Ω_1 is convex.

Remark 2.1 (Units)**.** For simplicity, we assume that the equations are written in non-dimensional form. Otherwise, the units are $[m \cdot s^{-1}]$ for $\boldsymbol{u}$, $[Pa]$ for $\boldsymbol{\sigma}$, $[Pa \cdot s]$ for μ, $[m^{-1}]$ for H_Γ and $[Pa \cdot m]$ for γ.

3. **Unfitted HHO solver with fixed interface**

This section briefly describes the unfitted HHO solver for the Stokes interface problem (2.1). The interface Γ is kept fixed in this section.

3.1. **Unfitted meshes**

We consider a mesh $\mathcal{T}$ belonging to a shape-regular mesh sequence such that each mesh covers Ω exactly. We denote by T a generic mesh cell having diameter h_T and unit outward normal $\boldsymbol{n}_T$. The mesh faces are collected in the set $\mathcal{F}$, which is split as $\mathcal{F} = \mathcal{F}^o \cup \mathcal{F}^\partial$, where $\mathcal{F}^o$ (resp. $\mathcal{F}^\partial$) is the collection of the mesh internal faces (resp. boundary faces). For all $T \in \mathcal{T}$, the faces composing the boundary of T are collected in the set $\mathcal{F}_{\partial T} := \{F \in \mathcal{F} : F \subset \partial T\}$.

Since the mesh is unfitted, the interface Γ can cut arbitrarily through some of the mesh cells. Thus, we partition $\mathcal{T}$ into $\mathcal{T} = \mathcal{T}^1 \cup \mathcal{T}^2 \cup \mathcal{T}^\Gamma$ with

$$\mathcal{T}^i := \{T \in \mathcal{T} : T \subset \Omega_i\}, \ i \in \{1,2\}, \quad \mathcal{T}^\Gamma := \{T \in \mathcal{T} : T \cap \Gamma \neq \emptyset\}, \tag{3.1}$$

and we introduce the notation

$$T^i := T \cap \Omega_i, \quad (\partial T)^i := \partial T \cap (\Omega_i \cup \partial\Omega), \quad i \in \{1,2\}, \quad T^\Gamma := T \cap \Gamma, \tag{3.2}$$

so that $\partial T^i = (\partial T)^i \cup T^\Gamma$. See Figure 3.1 for an example. The mesh cells belonging to the set $\mathcal{T}^\Gamma$ are called cut cells, and those belonging to the set $\mathcal{T}^1 \cup \mathcal{T}^2$ are called uncut cells. Consistently with the cell notation, we define $F^i := F \cap \Omega_i$ and $\mathcal{F}_{(\partial T)^i} := \{F^i : F \in \mathcal{F}_{\partial T}\}$. For simplicity, we assume that the interface does not intersect a vertex of a mesh cell and that $|\partial T \cap \Gamma| = 0$ for all $T \in \mathcal{T}^\Gamma$. These pathological situations, which can in principle be handled by specific geometrical coding procedures, were not encountered in our simulations.
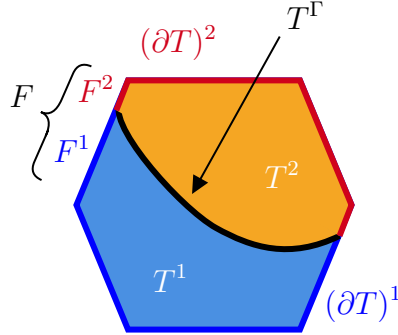

FIGURE 3.1. Decomposition of a cut cell $T \in \mathcal{T}^\Gamma$ and of its boundary ∂T.

3.2. **HHO discretization**

Let S be a subset of Ω of dimension $d' \in \{d-1, d\}$ (typically, S can be a mesh cell, a mesh face, or a collection thereof). For all $l \in \mathbb{N}$, we define $\mathbb{P}_{d'}^l(S)$ to be the space composed of d'-variate polynomials of total degree at most l restricted to S. Similarly, we use the notation $\mathbb{P}_{d'}^l(S; \mathbb{R}^d)$ and $\mathbb{P}_{d'}^l(S; \mathbb{R}_{\text{sym}}^{d \times d})$ for the space composed of d'-variate $\mathbb{R}^d$-valued and $\mathbb{R}_{\text{sym}}^{d \times d}$-valued polynomials of total degree at most l restricted to S, respectively, where $\mathbb{R}_{\text{sym}}^{d \times d}$ denotes the space of symmetric matrices of order d. Moreover, $(\cdot, \cdot)_S$

and $\|\cdot\|_S$ denote, respectively, the $L^2(S)$-inner product and the associated norm with d'-dimensional Lebesgue measure.

To discretize (2.1), we introduce a local HHO(k) space of order $k \geq 0$ for every mesh cell $T \in \mathcal{T}$. If the mesh cell $T \in \mathcal{T}$ is not cut by the interface Γ, the discrete velocity unknowns in T are a vector-valued polynomial of degree $(k+1)$ in the cell T and a vector-valued polynomial of degree k on each face $F \in \mathcal{F}_{\partial T}$, whereas the discrete pressure is a polynomial of order k in the cell T. Thus, the local HHO unknowns for the velocity and the pressure are

$$\widehat{\boldsymbol{v}}_T := (\boldsymbol{v}_T, \boldsymbol{v}_{\partial T}) \in \widehat{\boldsymbol{U}}_T^k := \mathbb{P}_d^{k+1}(T; \mathbb{R}^d) \times \mathbb{P}_{d-1}^k(\mathcal{F}_{\partial T}; \mathbb{R}^d), \tag{3.3a}$$

$$p_T \in P_T^k := \mathbb{P}_d^k(T), \tag{3.3b}$$

with $\mathbb{P}_{d-1}^k(\mathcal{F}_{\partial T}; \mathbb{R}^d) := \times_{F \in \mathcal{F}_{\partial T}} \mathbb{P}_{d-1}^k(F; \mathbb{R}^d)$. If, instead, the mesh cell $T \in \mathcal{T}$ is cut by the interface Γ, the idea is to double the unknowns in the cut cell and on its cut faces without attaching any unknowns to the interface. The local HHO unknowns for the velocity and the pressure are then

$$\widehat{\boldsymbol{v}}_T := (\boldsymbol{v}_{T^1}, \boldsymbol{v}_{T^2}, \boldsymbol{v}_{(\partial T)^1}, \boldsymbol{v}_{(\partial T)^2}) \in \widehat{\boldsymbol{U}}_T^k, \tag{3.4a}$$

$$p_T := (p_{T^1}, p_{T^2}) \in P_T^k := \mathbb{P}_d^k(T^1) \times \mathbb{P}_d^k(T^2), \tag{3.4b}$$

with

$$\widehat{\boldsymbol{U}}_T^k := \mathbb{P}_d^{k+1}(T^1; \mathbb{R}^d) \times \mathbb{P}_d^{k+1}(T^2; \mathbb{R}^d) \times \mathbb{P}_{d-1}^k(\mathcal{F}_{(\partial T)^1}; \mathbb{R}^d) \times \mathbb{P}_{d-1}^k(\mathcal{F}_{(\partial T)^2}; \mathbb{R}^d), \tag{3.5}$$

and $\mathbb{P}_{d-1}^k(\mathcal{F}_{(\partial T)^i}; \mathbb{R}^d) := \times_{F \in \mathcal{F}_{(\partial T)^i}} \mathbb{P}_{d-1}^k(F; \mathbb{R}^d)$ for all $i \in \{1, 2\}$. See Figure 3.2 for a representation of
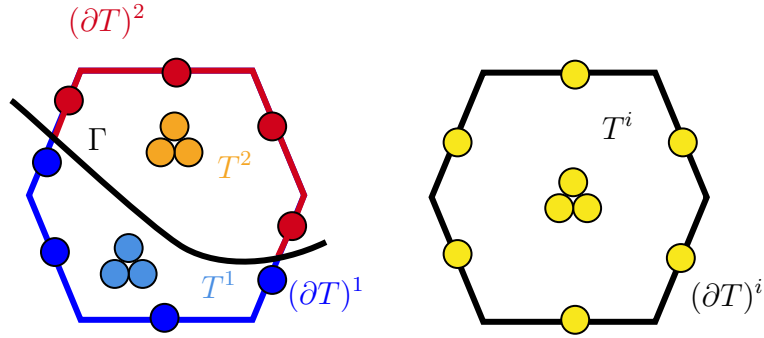

FIGURE 3.2. Discrete velocity unknowns ($k = 0$) for a cut (left) and uncut (right) cell of hexagonal shape. Notice the doubling of the cell unknowns in the cut cell and of the face unknowns on the cut faces. Conventionally, each bullet represents one $\mathbb{R}^2$-valued degree of freedom.

the discrete velocity unknowns in a cut and an uncut cell of hexagonal shape. To handle uncut and cut cells in a single formalism, we set for every uncut cell $T \in \mathcal{T}^i$ with $i \in \{1, 2\}$,

$$T^i := T, \quad T^{\bar{\imath}} := \emptyset, \quad (\partial T)^{\bar{\imath}} := \emptyset, \quad T^\Gamma := \emptyset, \tag{3.6}$$

where $\bar{\imath} := 3 - i$ (so that $\bar{1} := 2$ and $\bar{2} := 1$). We use a similar convention for the mesh faces.

Inspired by [9, 10], we define, for every mesh cell $T \in \mathcal{T}$ and all $i \in \{1, 2\}$, the symmetric gradient reconstruction operators $\mathbb{E}_{T^i}^k : \widehat{\boldsymbol{U}}_T^k \to \mathbb{P}_d^k(T^i; \mathbb{R}_{\text{sym}}^{d \times d})$, $i \in \{1, 2\}$, such that for all $\widehat{\boldsymbol{v}}_T \in \widehat{\boldsymbol{U}}_T^k$,

$$(\mathbb{E}_{T^i}^k(\widehat{\boldsymbol{v}}_T), \mathbf{q})_{T^i} := (\nabla^s \boldsymbol{v}_{T^i}, \mathbf{q})_{T^i} + (\boldsymbol{v}_{(\partial T)^i} - \boldsymbol{v}_{T^i}, \mathbf{q}\boldsymbol{n}_T)_{(\partial T)^i} - \alpha_i([\![\boldsymbol{v}_T]\!], \mathbf{q}\boldsymbol{n}_\Gamma)_{T^\Gamma}, \tag{3.7}$$

for all $\mathbf{q} \in \mathbb{P}_d^k(T^i; \mathbb{R}_{\text{sym}}^{d \times d})$. In the same spirit as in [9] for elliptic problems, robustness with respect to the contrast in the viscosity coefficients can be obtained defining

$$\alpha_i := \frac{\mu_{\bar{\imath}}}{\mu_i + \mu_{\bar{\imath}}}, \tag{3.8}$$

so that $\alpha_1 = \alpha_2 = 0.5$ if $\mu_1 = \mu_2$, whereas $\alpha_1 \approx 0$, $\alpha_2 \approx 1$ if $\mu_1 \gg \mu_2$ and vice versa if $\mu_2 \gg \mu_1$. Similarly, the divergence reconstruction operator $D_{T^i}^k : \widehat{\boldsymbol{U}}_T^k \to \mathbb{P}_d^k(T^i)$ is such that, for all $\widehat{\boldsymbol{v}}_T \in \widehat{\boldsymbol{U}}_T^k$,

$$D_{T^i}^k(\widehat{\boldsymbol{v}}_T) := \operatorname{trace}(\mathbb{E}_{T^i}^k(\widehat{\boldsymbol{v}}_T)). \tag{3.9}$$

Then, the local HHO bilinear and linear forms are defined as follows: For all $(\widehat{\boldsymbol{v}}_T, r_T)$, $(\widehat{\boldsymbol{w}}_T, q_T) \in \widehat{\boldsymbol{U}}_T^k \times P_T^k$,

$$A_T((\widehat{\boldsymbol{v}}_T, r_T), (\widehat{\boldsymbol{w}}_T, q_T)) := a_T(\widehat{\boldsymbol{v}}_T, \widehat{\boldsymbol{w}}_T) - b_T(\widehat{\boldsymbol{w}}_T, r_T) + b_T(\widehat{\boldsymbol{v}}_T, q_T), \tag{3.10a}$$

$$l_T(\widehat{\boldsymbol{w}}_T) := \sum_{i \in \{1,2\}} \left\{ (\boldsymbol{f}, \boldsymbol{w}_{T^i})_{T^i} + \alpha_{\bar{i}}(\boldsymbol{g}_N, \boldsymbol{w}_{T^i})_{T^\Gamma} \right\}, \tag{3.10b}$$

with the bilinear forms

$$a_T(\widehat{\boldsymbol{v}}_T, \widehat{\boldsymbol{w}}_T) := \sum_{i \in \{1,2\}} 2\mu_i (\mathbb{E}_{T^i}^k(\widehat{\boldsymbol{v}}_T), \mathbb{E}_{T^i}^k(\widehat{\boldsymbol{w}}_T))_{T^i} + s_T^\Gamma(\widehat{\boldsymbol{v}}_T, \widehat{\boldsymbol{w}}_T) + s_T^{1,2}(\widehat{\boldsymbol{v}}_T, \widehat{\boldsymbol{w}}_T), \tag{3.11a}$$

$$b_T(\widehat{\boldsymbol{w}}_T, r_T) := \sum_{i \in \{1,2\}} (r_{T^i}, D_{T^i}^k(\widehat{\boldsymbol{w}}_T))_{T^i}, \tag{3.11b}$$

and the following stabilization bilinear forms:

$$s_T^\Gamma(\widehat{\boldsymbol{v}}_T, \widehat{\boldsymbol{w}}_T) := \mu_\# h_T^{-1}([\![\boldsymbol{v}_T]\!], [\![\boldsymbol{w}_T]\!])_{T^\Gamma}, \qquad \mu_\# := \min(\mu_1, \mu_2), \tag{3.12a}$$

$$s_T^{1,2}(\widehat{\boldsymbol{v}}_T, \widehat{\boldsymbol{w}}_T) := \sum_{i \in \{1,2\}} \mu_i h_T^{-1}(\Pi_{(\partial T)^i}^k(\boldsymbol{v}_{T^i}) - \boldsymbol{v}_{(\partial T)^i}, \Pi_{(\partial T)^i}^k(\boldsymbol{w}_{T^i}) - \boldsymbol{w}_{(\partial T)^i})_{(\partial T)^i}. \tag{3.12b}$$

The operator $\Pi_{(\partial T)^i}^k$ denotes the L^2-orthogonal projection onto $\mathbb{P}_{d-1}^k(\mathcal{F}_{(\partial T)^i}; \mathbb{R}^d)$. Notice that an additional stabilization (with a small enough parameter) is considered in [10] for theoretical reasons, but the numerical results therein indicate that this stabilization can be omitted. We do not consider it in this work.

Passing to the global setting, we define for all $i \in \{1, 2\}$,

$$\boldsymbol{U}_{\mathcal{T}^i}^{k+1} := \underset{T \in \mathcal{T}}{\times} \mathbb{P}_d^{k+1}(T^i; \mathbb{R}^d), \qquad \boldsymbol{U}_{\mathcal{F}^i}^k := \underset{F \in \mathcal{F}}{\times} \mathbb{P}_{d-1}^k(F^i; \mathbb{R}^d), \tag{3.13a}$$

$$P_{\mathcal{T}^i}^k := \underset{T \in \mathcal{T}}{\times} \mathbb{P}_d^k(T^i). \tag{3.13b}$$

We define the following spaces for the global HHO unknowns:

$$\widehat{\boldsymbol{U}}_{\mathcal{T}}^k := \boldsymbol{U}_{\mathcal{T}^1}^{k+1} \times \boldsymbol{U}_{\mathcal{T}^2}^{k+1} \times \boldsymbol{U}_{\mathcal{F}^1}^k \times \boldsymbol{U}_{\mathcal{F}^2}^k, \qquad P_{\mathcal{T}}^k := P_{\mathcal{T}^1}^k \times P_{\mathcal{T}^2}^k. \tag{3.14}$$

For all $\widehat{\boldsymbol{v}}_{\mathcal{T}} \in \widehat{\boldsymbol{U}}_{\mathcal{T}}^k$, we write $\widehat{\boldsymbol{v}}_{\mathcal{T}} = (\boldsymbol{v}_{\mathcal{T}^1}, \boldsymbol{v}_{\mathcal{T}^2}, \boldsymbol{v}_{\mathcal{F}^1}, \boldsymbol{v}_{\mathcal{F}^2})$ and for all $q_{\mathcal{T}} \in P_{\mathcal{T}}^k$, we write $q_{\mathcal{T}} = (q_{\mathcal{T}^1}, q_{\mathcal{T}^2})$. Moreover, for all $T \in \mathcal{T}$, we denote by

$$\widehat{\boldsymbol{v}}_T := (\boldsymbol{v}_{T^1}, \boldsymbol{v}_{T^2}, \boldsymbol{v}_{(\partial T)^1}, \boldsymbol{v}_{(\partial T)^2}) \in \widehat{\boldsymbol{U}}_T^k, \quad q_T = (q_{T^1}, q_{T^2}) \in P_T^k, \tag{3.15}$$

the local components of $\widehat{\boldsymbol{v}}_{\mathcal{T}}$ and $q_{\mathcal{T}}$, respectively, attached to the mesh cell T and its faces. We denote by $\widehat{\boldsymbol{U}}_{\mathcal{T}0}^k$ the subspace of $\widehat{\boldsymbol{U}}_{\mathcal{T}}^k$ where all the velocity components attached to the boundary faces composing $\partial\Omega$ are null and by $P_{\mathcal{T}*}^k$ the subspace of $P_{\mathcal{T}}^k$ composed of functions with zero average over Ω. Finally, defining the global bilinear and linear forms

$$A_{\mathcal{T}}((\widehat{\boldsymbol{v}}_{\mathcal{T}}, r_{\mathcal{T}}), (\widehat{\boldsymbol{w}}_{\mathcal{T}}, q_{\mathcal{T}})) := \sum_{T \in \mathcal{T}} A_T((\widehat{\boldsymbol{v}}_T, r_T), (\widehat{\boldsymbol{w}}_T, q_T)), \tag{3.16a}$$

$$L_{\mathcal{T}}(\widehat{\boldsymbol{w}}_{\mathcal{T}}) := \sum_{T \in \mathcal{T}} l_T(\widehat{\boldsymbol{w}}_T), \tag{3.16b}$$

263

the discrete problem amounts to seeking $(\widehat{\boldsymbol{u}}_{\mathcal{T}}, p_{\mathcal{T}}) \in \widehat{\boldsymbol{U}}_{\mathcal{T}0}^k \times P_{\mathcal{T}*}^k$ such that

$$A_{\mathcal{T}}((\widehat{\boldsymbol{u}}_{\mathcal{T}}, p_{\mathcal{T}}), (\widehat{\boldsymbol{w}}_{\mathcal{T}}, q_{\mathcal{T}})) = L_{\mathcal{T}}(\widehat{\boldsymbol{w}}_{\mathcal{T}}), \qquad \forall (\widehat{\boldsymbol{w}}_{\mathcal{T}}, q_{\mathcal{T}}) \in \widehat{\boldsymbol{U}}_{\mathcal{T}0}^k \times P_{\mathcal{T}*}^k. \tag{3.17}$$

The error analysis for the discrete problem (3.17) is performed in [10] by establishing inf-sup stability, consistency, and approximation properties. (Therein, the parameters α_i are such that $\alpha_i = 0$ if $\mu_i \leq \mu_{\bar{\imath}}$, but the adaptation of the analysis to the parameters α_i prescribed as in (3.8) is straightforward.) A key tool for the analysis is to ensure, by means of the cell agglomeration procedure described in [9, Section 4.3], that any cut cell $T \in \mathcal{T}^{\Gamma}$ satisfies $\min_{i \in \{1,2\}} |T^i| \geq \varrho|T|$ for a given user-parameter $\varrho \in (0, \frac{1}{2})$ (hereafter, we use $\varrho := 0.3$ consistently with [9]). Then, assuming that $(\boldsymbol{u}_i, p_i) \in H^{k+2}(\Omega_i; \mathbb{R}^d) \times H^{k+1}(\Omega_i)$, $i \in \{1, 2\}$, [10, Theorem 12] states that there is a constant C, independent of the mesh-size $h := \max_{T \in \mathcal{T}} h_T$ and of the fluid viscosities μ_i, $i \in \{1, 2\}$, such that

$$\left\{ \sum_{T \in \mathcal{T}} \sum_{i \in \{1,2\}} \mu_i \|\nabla^{\mathrm{s}}(\boldsymbol{u}_i - \boldsymbol{u}_{T^i})\|_{T^i}^2 + \mu_i^{-1} \|p_i - p_{T^i}\|_{T^i}^2 \right\}^{\frac{1}{2}}$$

$$\leq Ch^{k+1} \left\{ \sum_{i \in \{1,2\}} \mu_i |\boldsymbol{u}_i|_{H^{k+2}(\Omega_i; \mathbb{R}^d)}^2 + \mu_i^{-1} \|p_i\|_{H^{k+1}(\Omega_i)}^2 \right\}^{\frac{1}{2}}. \tag{3.18}$$

3.3. Interface discretization and quadratures in the cut cells

An important novelty of the present work with respect to [9, 10] is that the interface Γ is no longer considered to be analytically known. Instead, it is known here only through a discrete approximation $\phi_{\mathcal{T}}$ of the level-set function ϕ introduced in (2.6). Thus, we set

$$\Gamma_{\mathcal{T}} := \{\boldsymbol{x} \in \Omega : \phi_{\mathcal{T}}(\boldsymbol{x}) = 0\}. \tag{3.19}$$

The construction of the discrete approximation $\phi_{\mathcal{T}}$ is discussed in Section 5.

In practice, the interface $\Gamma_{\mathcal{T}}$ is approximately represented by a collection of arcs, each arc being generated from the reference interval $\widehat{I} := [0, 1]$ by using a geometric mapping whose components are polynomial-valued. Specifically, for every cut cell $T \in \mathcal{T}^{\Gamma}$, $\Gamma_{\mathcal{T}} \cap T$ is approximated by a collection of 2^n arcs, where $n \geq 0$ is a user-specified parameter. These arcs are denoted by $\Upsilon^{T,j}$, $j \in \{1:2^n\}$. To build each arc $\Upsilon^{T,j}$, we consider $(l+1)$ equidistributed interpolation nodes $\{\boldsymbol{x}_m^{T,j}\}_{m \in \{0:l\}} \subset \Gamma_{\mathcal{T}}$. The construction of these nodes is discussed below. The integer l is a user-specified parameter such that $l \geq k+1$, where k is the degree of the face unknowns in the HHO method. This lower bound is coherent with the consistency analysis of elliptic problems on curved domains, where the geometry error is at least one order higher than the approximation error in the H^1-norm (which is of order $(k+1)$ for the HHO method).

Considering the Lagrange basis of order l, $\{\widehat{\psi}_m\}_{m \in \{0:l\}}$, defined on the reference interval $\widehat{I}$ using equidistributed nodes, the arc $\Upsilon^{T,j}$ is defined as

$$\Upsilon^{T,j} := \boldsymbol{r}^{T,j}(\widehat{I}) \qquad \text{where} \qquad \boldsymbol{r}^{T,j}(\widehat{s}) := \sum_{m \in \{0:l\}} \boldsymbol{x}_m^{T,j} \widehat{\psi}_m(\widehat{s}), \quad \forall \widehat{s} \in \widehat{I}. \tag{3.20}$$

Finally, the fully discrete interface is defined as follows:

$$\Gamma_{\mathcal{T}}^{n,l} := \bigcup_{T \in \mathcal{T}^{\Gamma}} \bigcup_{j \in \{1:2^n\}} \Upsilon^{T,j}. \tag{3.21}$$

We notice that the fully discrete interface has only C^0-regularity. An interesting perspective, left to future work, is to study whether a smooth discrete interface, e.g., built using splines to achieve C^1-regularity, can have a sizable effect in improving solution accuracy.

To construct the interpolation nodes $\{\boldsymbol{x}_m^{T,j}\}_{m\in\{0:l\}}$ for all $T \in \mathcal{T}^\Gamma$ and all $j \in \{1:2^n\}$, we assume for simplicity that the interface Γ intersects ∂T at two points only and that these points are located on two distinct edges of T. Let us denote by $\boldsymbol{a}_0$ and $\boldsymbol{a}_{2^n l}$ the two intersection points, ordered according to the orientation of Γ (see Figure 2.1). We proceed as follows (see Figure 3.3):

(1) Construction of the points $\{\boldsymbol{a}_{jl}\}_{j\in\{0:2^n\}}$, all lying on $\Gamma_\mathcal{T}$. If $n = 0$, there is nothing to do. Otherwise, $n \geq 1$ and the points $\{\boldsymbol{a}_{jl}\}_{j\in\{0:2^n\}}$ are constructed recursively. Let $m \in \{1:n\}$ and assume that the points $\{\boldsymbol{a}_{k2^{n-m+1}l}\}_{k\in\{0:2^{m-1}\}}$ are available (all on $\Gamma_\mathcal{T}$). Then we construct the points $\{\boldsymbol{a}_{(2k+1)2^{n-m}l}\}_{k\in\{0:2^{m-1}-1\}}$ as follows. For all $k \in \{0:2^{m-1}\}$, we let $\bar{\boldsymbol{x}}_k$ be the midpoint of the segment $[\boldsymbol{a}_{k2^{n-m+1}l}, \boldsymbol{a}_{(k+1)2^{n-m+1}l}] := \{(1-\theta)\boldsymbol{a}_{k2^{n-m+1}l} + \theta\boldsymbol{a}_{(k+1)2^{n-m+1}l}, \theta \in [0,1]\}$, and L_k be the line passing through $\bar{\boldsymbol{x}}_k$ and orthogonal to this segment. We define $\boldsymbol{a}_{(2k+1)2^{n-m}l}$ to be the closest point in L_k to $\bar{\boldsymbol{x}}_k$ such that $\phi_\mathcal{T}(\boldsymbol{a}_{(2k+1)2^{n-m}l}) = 0$, i.e., $\boldsymbol{a}_{(2k+1)2^{n-m}l} \in \Gamma_\mathcal{T}$. This point is found by dichotomy.

(2) For all $j \in \{0:2^n - 1\}$, we now construct the points $\{\boldsymbol{a}_{jl+m}\}_{m\in\{1:l-1\}}$ as follows. We consider the segment $[\boldsymbol{a}_{jl}, \boldsymbol{a}_{(j+1)l}] := \{(1-\theta)\boldsymbol{a}_{jl} + \theta\boldsymbol{a}_{(j+1)l}, \theta \in [0,1]\}$. For all $m \in \{1:l-1\}$, we set $\bar{\boldsymbol{x}}_m := (1-\theta_m)\boldsymbol{a}_{jl} + \theta_m\boldsymbol{a}_{(j+1)l}$ with $\theta_m := m/l$, we let L_m be the line passing through $\bar{\boldsymbol{x}}_m$ and orthogonal to this segment, and we define $\boldsymbol{a}_{jl+m}$ to be the closest point in L_m to $\bar{\boldsymbol{x}}_m$ such that $\phi_\mathcal{T}(\boldsymbol{a}_{jl+m}) = 0$, i.e., $\boldsymbol{a}_{jl+m} \in \Gamma_\mathcal{T}$. This point is found by dichotomy.

(3) We have now built the collection of points $\{\boldsymbol{a}_j\}_{j\in\{0:2^n l\}}$, all in $\Gamma_\mathcal{T}$. Finally, we set

$$\boldsymbol{x}_m^{T,j} := \boldsymbol{a}_{(j-1)l+m}, \quad j \in \{1:2^n\}, \, m \in \{0:l\}. \tag{3.22}$$

Notice that $\boldsymbol{x}_l^{T,j} = \boldsymbol{x}_0^{T,j+1}$ by construction, ensuring the matching of the endpoint of each arc with the starting point of the next arc.
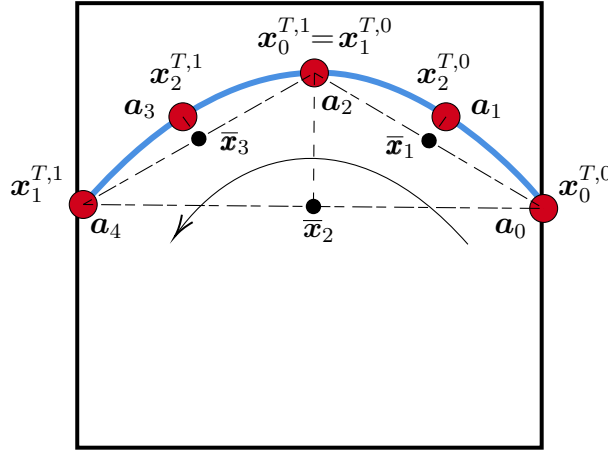

FIGURE 3.3. Example of a square cut cell $T \in \mathcal{T}^\Gamma$ with interface (blue line) and interface points (red bullets) $\{\boldsymbol{x}_m^{T,j}\}_{m\in\{0:l\}}$, $j \in \{1:2^n\}$. The interface discretization parameters are ($l = 2$, $n = 0$). The construction of the points $\boldsymbol{a}_m$ and $\bar{\boldsymbol{x}}_m$, for all $m \in \{0:2^n l\}$, is shown. The arrow indicates the interface orientation.

To realize the unfitted HHO method, high-order quadratures need to be performed along the fully discrete interface $\Gamma_\mathcal{T}^{n,l}$ and in the cut cells (for the uncut cells, the procedure is straightforward). One-dimensional quadratures along $\Gamma_\mathcal{T}^{n,l}$ are straightforward to implement by using the above geometric

mappings. Moreover, to implement quadratures in the cut cells, we decompose T^i, $i \in \{1, 2\}$, into curved subtriangles which are mapped into a reference triangle where quadratures based on Dunavant points are performed. The construction of geometric nonaffine mappings based on sets of geometric nodes is described, e.g., in [19, Section 8.1]. The whole procedure in a cut cell is illustrated in Figure 3.4. We emphasize that substantial computational savings are achieved compared to [10] where quadratures are realized using a very large number of flat triangles ($n \gg 1$, $l = 1$).

a. The interface cuts two adjacent faces of T and leaves one vertex in T^i.

b. The interface cuts two adjacent faces of T and leaves three vertices in T^i.

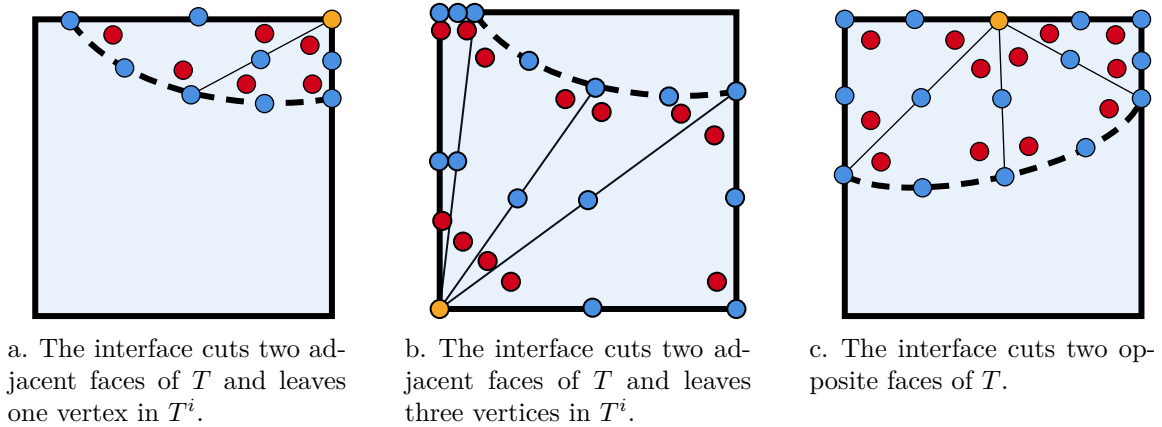c. The interface cuts two opposite faces of T.

FIGURE 3.4. Example of cut cells $T \in \mathcal{T}^\Gamma$ and of their decomposition into curved subtriangles. The subtriangulation is performed by connecting the interface points $\{\boldsymbol{x}_m^{T,j}\}_{m\in\{0:2\}}$, $j \in \{1:2^n\}$ to a specific point (orange bullet, a vertex or an edge midpoint according to the cut configuration). The interface discretization parameters are ($l = 2$, $n = 1$). The blue bullets, plus the orange bullet, are the physical points used for defining the mapping from the reference triangle into the physical one (quadratic mapping in the present example). Moreover, the red bullets represent the mapped integration Dunavant points for the second-order quadrature.

4. Equilibrium with a pure shear flow

In this section, the interface is kept fixed, i.e., we solve the Stokes interface problem (2.1). Specifically we study the shear-surface tension equilibrium problem in the absence of body forces, i.e., $\boldsymbol{f}_i := \boldsymbol{0}$, $i \in \{1, 2\}$. Let the box $\Omega := (-a, a)^2$, $a > 0$, be the computational domain. We consider the following non-homogeneous Dirichlet condition enforcing a pure shear flow on $\partial\Omega$:

$$\boldsymbol{g} := \boldsymbol{u}_{\varepsilon|\partial\Omega} \qquad \text{where} \qquad \boldsymbol{u}_\varepsilon(x, y) := \varepsilon(x, -y)^{\mathrm{T}}, \tag{4.1}$$

with the shear parameter $\varepsilon > 0$. In the limit $a \to \infty$, the interface is elliptic of radii $0 < R_1 \leq R_2$ [15, 38]. It is convenient to define the Taylor deformation parameter

$$D := \frac{R_2 - R_1}{R_1 + R_2}. \tag{4.2}$$

We also define the capillary number

$$Ca := \mu_2 \frac{\varepsilon L_*}{\gamma}, \tag{4.3}$$

where the shear parameter ε is prescribed by (4.1) and, consistently with Taylor's study dealing with the deformation of an initial circular droplet, the reference length scale L_* is defined as

$$L_* := 2R_* \qquad \text{with} \qquad R_* := \sqrt{\frac{|\Omega_1|}{\pi}} = \sqrt{R_1 R_2}. \tag{4.4}$$

Putting everything together, the capillary number reads

$$Ca := 2\mu_2 \frac{\varepsilon \sqrt{R_1 R_2}}{\gamma}. \tag{4.5}$$

Notice that one needs to prescribe one additional length scale to uniquely solve the problem; for instance, one can prescribe the reference length scale L_* or the radius of the inner subdomain R_1.

In the limit case where $\varepsilon = 0$ (i.e., null shear), the equilibrium interface has a circular form, i.e., $D = 0$ meaning that $R_1 = R_2$. Whenever $\varepsilon > 0$, the equilibrium interface has an elliptic shape: the shear flow stretches the interface along the x-axis and compresses it along the y-axis. Figure 4.1 shows the streamlines of the equilibrium velocity field with shear $\varepsilon = 0.59$ and radii $R_1 = 1/6$ and $R_2 = 1/3$ (so that $D = 1/3$ and $R_* = 1/(3\sqrt{2})$).
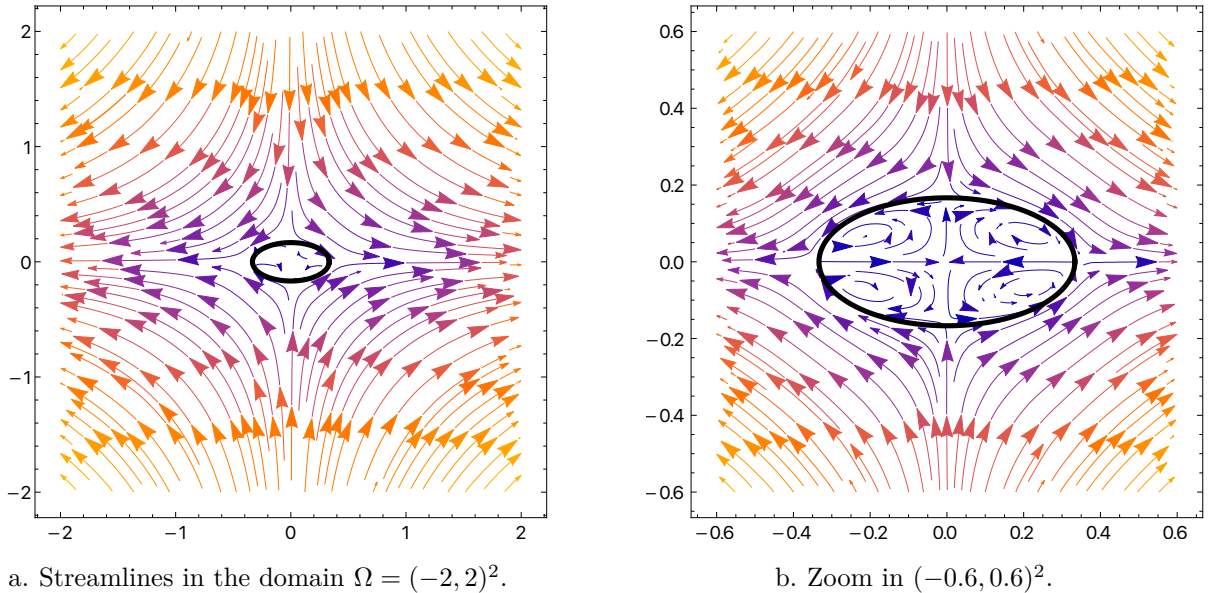

a. Streamlines in the domain $\Omega = (-2,2)^2$. b. Zoom in $(-0.6, 0.6)^2$.

FIGURE 4.1. Streamlines of the velocity field $\boldsymbol{u}$ obtained by solving (2.5) with $\gamma = 1$, $\mu_1 = \mu_2 = 1$ in the domain $\Omega = (-2,2)^2$, employing the unfitted HHO discretization with polynomial order $k = 1$. The shear parameter is $\varepsilon = 0.59$. The domain is discretized by a mesh composed of 128×128 square cells. The ellipse has radii $R_1 = 1/6$, $R_2 = 1/3$.

Our goal is to study numerically the capillary number Ca leading to equilibrium. In the first part of our study, we fix $\mu_1 = \mu_2 = 1$, and we fix an elliptic interface having radii R_1 and R_2, thus prescribing the value of the Taylor deformation parameter D. We want to find numerically the ratio $m_{\text{eq}} := \frac{\varepsilon_{\text{eq}}}{\gamma_{\text{eq}}}$ leading to equilibrium. Owing to the linearity of the Stokes interface problem (2.1), the velocity field $\boldsymbol{u}(\varepsilon, \gamma)$ depends linearly on ε and γ, so that we have

$$\boldsymbol{u}(\varepsilon, \gamma) = \boldsymbol{u}(\varepsilon, 0) + \boldsymbol{u}(0, \gamma), \tag{4.6}$$

where $\boldsymbol{u}(\varepsilon, 0)$ depends linearly on ε and $\boldsymbol{u}(0, \gamma)$ depends linearly on γ. Notice in passing that $\boldsymbol{u}(\varepsilon, 0)$ differs from $\boldsymbol{u}_\varepsilon$ when the viscosities of the two fluids are not equal. The key observation is that, since

the equilibrium of the interface is achieved when the normal velocity at the interface is null, we must have

$$\frac{\boldsymbol{u}(\varepsilon_{\text{eq}}, 0) \cdot \boldsymbol{n}_\Gamma}{\boldsymbol{u}(0, \gamma_{\text{eq}}) \cdot \boldsymbol{n}_\Gamma} = -1 \qquad \text{a.e. on } \Gamma, \tag{4.7}$$

up to the few points on Γ where both numerator and denominator vanish. Therefore, the value of m_{eq} can be found by computing the two reference velocity fields $\boldsymbol{u}(0, \gamma = 1)$ and $\boldsymbol{u}(\varepsilon = 1, 0)$. These two reference velocity fields are such that their normal component at the interface are linearly correlated, i.e., we have

$$\frac{\boldsymbol{u}(0, \gamma = 1) \cdot \boldsymbol{n}_\Gamma}{\boldsymbol{u}(\varepsilon = 1, 0) \cdot \boldsymbol{n}_\Gamma} = -m_{\text{eq}} \qquad \text{a.e. on } \Gamma. \tag{4.8}$$

By determining the value of m_{eq}, one readily deduces from (4.3) the value of the capillary number Ca associated with the prescribed value of the Taylor deformation parameter D.
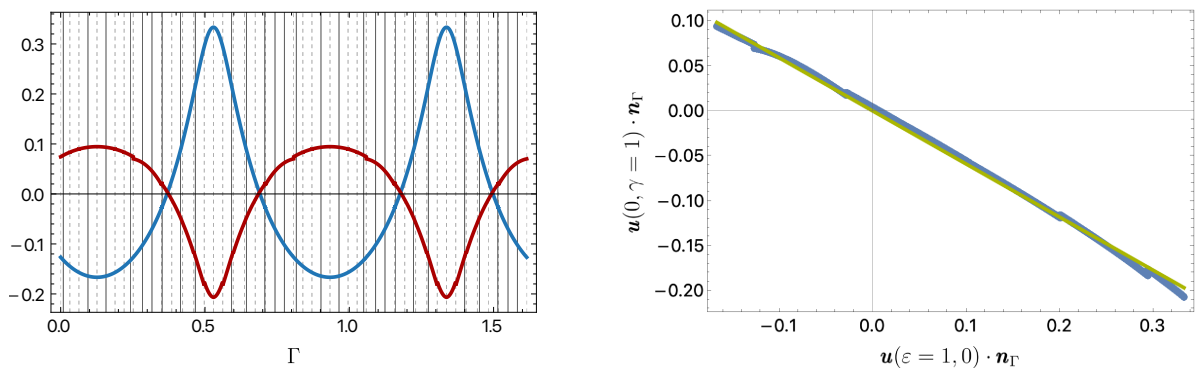
a. $\boldsymbol{u}(\varepsilon = 1, 0) \cdot \boldsymbol{n}_\Gamma$ (blue) and $\boldsymbol{u}(0, \gamma = 1) \cdot \boldsymbol{n}_\Gamma$ (red) along the interface.

b. $\boldsymbol{u}(0, \gamma = 1) \cdot \boldsymbol{n}_\Gamma$ w.r.t. $\boldsymbol{u}(\varepsilon = 1, 0) \cdot \boldsymbol{n}_\Gamma$.

FIGURE 4.2. Figure 4.2.a: normal velocities along the interface; the dashed vertical lines in the background represent the intersections between the interface and the cell faces, whereas the solid lines represent the intersections between the interface and the erased inner faces of the agglomerated cells. Figure 4.2.b: $\boldsymbol{u}(0, \gamma = 1) \cdot \boldsymbol{n}_\Gamma$ versus $\boldsymbol{u}(\varepsilon = 1, 0) \cdot \boldsymbol{n}_\Gamma$ (blue bullets); the green line represents the linear regression curve with slope $-m_{\text{eq}} \approx 0.590$. Elliptic interface with $D = 1/3$ and $\mu_1 = \mu_2 = 1$. The velocity fields $\boldsymbol{u}(\varepsilon = 1, 0)$ and $\boldsymbol{u}(0, \gamma = 1)$ are computed in the domain $\Omega = (-2, 2)^2$ discretized by a mesh composed of 128×128 square cells. We employ the unfitted HHO discretization with polynomial order $k = 1$.

Let us exemplify the procedure for the elliptic interface with radii $R_1 = 1/6$ and $R_2 = 1/3$ (so that $D = 1/3$ and $R_* = 1/(3\sqrt{2})$). Recall that $\mu_1 = \mu_2 = 1$. The computational domain is set to $\Omega = (-2, 2)^2$ and is initially discretized by 128×128 square cells. After using the cell-agglomeration procedure from [9], the mesh is composed of 16352 (instead of 16384) cells. We set the interface discretization parameters to ($l = 4$, $n = 0$). Figure 4.2.a shows the normal velocities $\boldsymbol{u}(\varepsilon = 1, 0) \cdot \boldsymbol{n}_\Gamma$ and $\boldsymbol{u}(0, \gamma = 1) \cdot \boldsymbol{n}_\Gamma$ along the interface Γ. Interestingly, the contribution of the jump of the viscous stress tensor tends to vanish at the interface, so that the pressure jump absorbs all the surface tension force. As Figure 4.2.b shows, the linear correlation between both normal components is rather well established numerically. The slope of the linear regression curve is $-m_{\text{eq}} \approx -0.590$. Therefore, in the case $D = 1/3$, $\mu_1 = \mu_2 = 1$, $\gamma = 1$, we conclude that the equilibrium is obtained for $\varepsilon_{\text{eq}} = -m_{\text{eq}}$, i.e.,

$$Ca = 2\varepsilon_{\text{eq}}\sqrt{R_1 R_2} \approx 0.278. \tag{4.9}$$

For this value, the peak normal flow velocity computed numerically at the interface is 1×10^{-2} (which can be considered to be reasonably close to zero). Figure 4.3 displays the normal velocity and the curvature along the interface for three meshes composed of 32×32, 64×64 and 128×128 square cells. Notice that peaks on normal velocities coincide with maximal curvature in absolute value. Using mesh refinement, the maximal normal velocity at the interface is reduced to 7×10^{-2}, 3×10^{-2} and 1×10^{-2}, respectively. Moreover, the three meshes lead to the values $\varepsilon_{\text{eq}} \in \{0.654, 0.581, 0.590\}$ and $Ca \in \{0.308, 0.274, 0.278\}$, indicating satisfactory convergence on the finest mesh. Notice that the interface discretization parameters (l, n) have a marginal influence on the accuracy of the numerical predictions. The only differences were observed for $(l = 1, n = 1)$ giving $Ca = 0.280$ and $(l = 1, n = 2)$ giving $Ca = 0.279$. All the other choices for $(l, n) \in \{1{:}6\} \times \{1{:}4\}$ give the same value for Ca as above. Figure 4.4 displays isocontours for the two velocity components of the equilibrium flow.

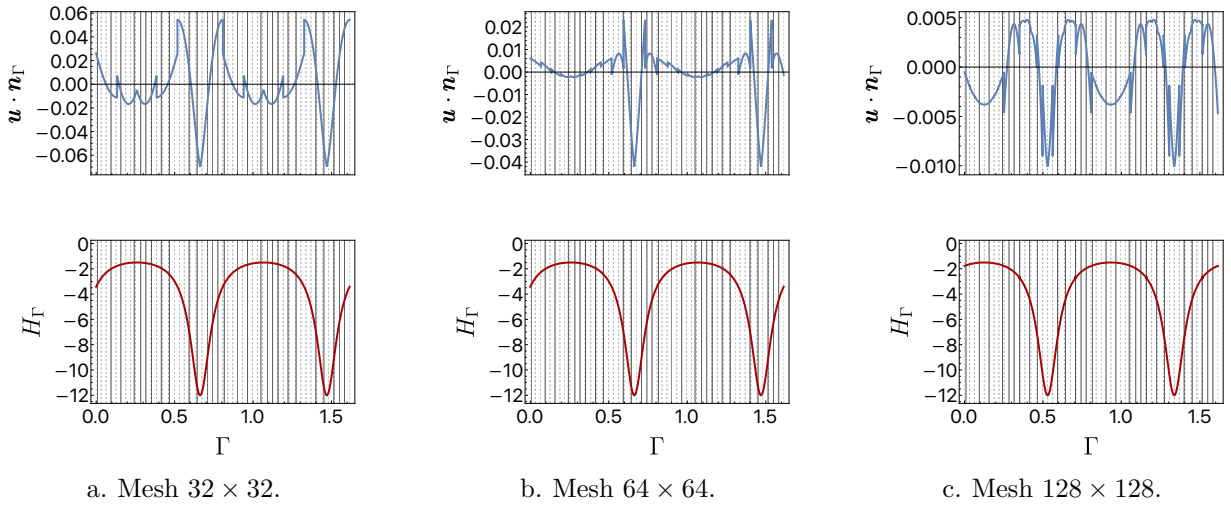a. Mesh 32×32. b. Mesh 64×64. c. Mesh 128×128.

FIGURE 4.3. Normal velocity (blue, top row) and curvature (red, bottom row) along the interface. Shear-surface tension equilibrium with elliptic interface for $D = 1/3$, $\mu_1 = \mu_2 = 1$, $Ca \in \{0.308, 0.274, 0.278\}$ using meshes composed of 32×32, 64×64 and 128×128 square cells, respectively (i.e., $\varepsilon \in \{0.654, 0.581, 0.590\}$, $\gamma = 1$, $R_1 = 1/6$ and $R_2 = 1/3$) in the domain $(-2, 2)^2$. We employ the unfitted HHO discretization with polynomial order $k = 1$.

A relevant numerical parameter is the size of the computational domain which has to be large enough so as not to affect the shear-surface tension equilibrium. To evaluate quantitatively the possible influence of this size on our results, we consider two additional computational domains, $\Omega_m := (-1, 1)^2$ and $\Omega_M := (-3, 3)^2$, still for $D = 1/3$ and $\mu_1 = \mu_2 = 1$. The mesh-size is the same for the three computational domains: this means using a mesh composed of 64×64 (resp., 128×128 and 192×192) square cells for Ω_m (resp., Ω and Ω_M). The predicted values of Ca are 0.246, 0.278 and 0.284 on Ω_m, Ω and Ω_M, respectively. We notice, as expected, that the difference between the predicted capillary numbers decreases by increasing the size of the computational domain owing to the minor influence of the external boundary.

It is interesting to study how the ratio D/Ca depends on the viscosity ratio

$$\lambda := \frac{\mu_1}{\mu_2}. \tag{4.10}$$

The results are summarized in Figure 4.5. In Figure 4.5.a, we present the results obtained for $D = 0.33$ on the three computational domains considered above to verify that our predictions are essentially
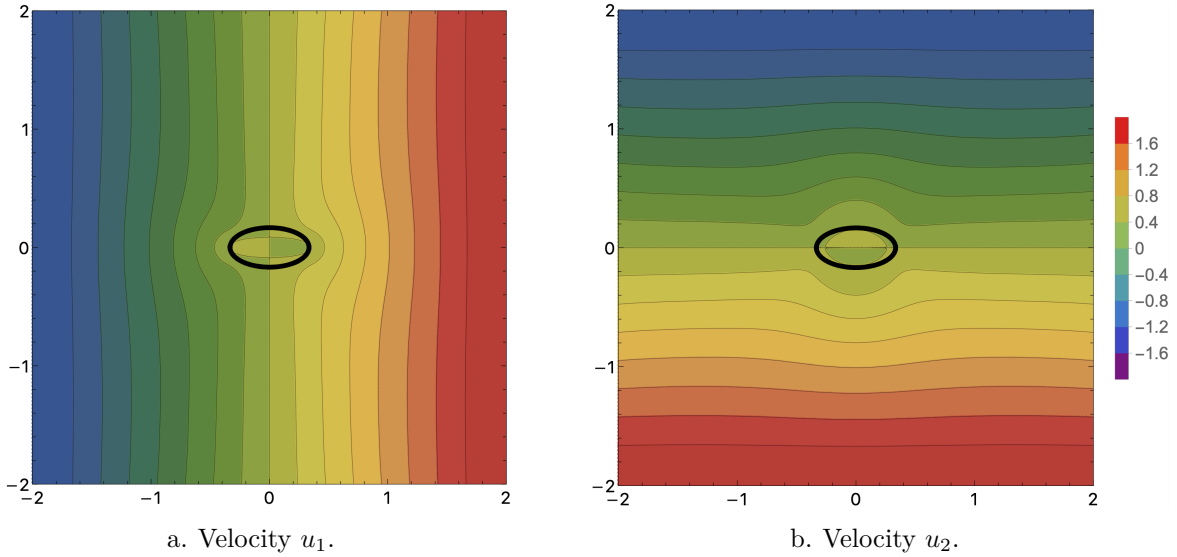
a. Velocity u_1.

b. Velocity u_2.

FIGURE 4.4. Shear-surface tension equilibrium with elliptic interface: isovalues of the velocity components $\boldsymbol{u} = (u_1, u_2)$ for $D = 1/3$, $\mu_1 = \mu_2 = 1$, $Ca = 0.28$ (i.e., $\varepsilon = 0.59$, $\gamma = 1$, $R_1 = 1/6$ and $R_2 = 1/3$) in the domain $\Omega = (-2, 2)^2$ discretized by a mesh composed of 128×128 square cells. We employ the unfitted HHO discretization with polynomial order $k = 1$.

independent of the size of Ω as long as $(-2, 2)^2 \subseteq \Omega$. In Figure 4.5.b, we fix $\Omega = (-2, 2)^2$ and we consider various values for the Taylor deformation parameter, $D \in \{0.01, 0.11, 0.20, 0.27, 0.31, 0.33\}$. Our results for small D are in reasonable agreement with the estimate from [38] which is indeed derived under the assumption of small deformations, i.e., when the shape of the interface only slightly departs from a circle. This estimate states that

$$D \approx Ca \frac{19\lambda + 16}{16\lambda + 16}. \tag{4.11}$$

The discrepancy between our simulations and (4.11) can be attributed to the fact that (4.11) appears to be derived from some analytical expressions for the velocity and pressure in a fully 3D (spherical) setting. Finally, in Figure 4.5.c, we plot D as a function of Ca for the above values of λ; the results are in good agreement with those reported in [38].

5. Fixed-point solver for unknown interface problems

This section describes the various ingredients composing the fixed-point solver used to solve numerically shear-surface tension equilibrium problems with unknown interface.

5.1. Fixed-point scheme

The mesh $\mathcal{T}$ is fixed during the whole iterative process and is therefore unfitted to the interface. For simplicity, we consider that the computational domain is a square and that the mesh is composed of square cells. The level-set function is discretized in the continuous finite element space

$$Q_q^{\mathrm{c}}(\mathcal{T}) := \{v_{\mathcal{T}} \in \mathcal{C}^0(\overline{\Omega}) : v_{\mathcal{T}|T} \in \mathbb{Q}_{q,d}, \ \forall T \in \mathcal{T}\}, \tag{5.1}$$

where $\mathbb{Q}_{q,d}$ denotes the space composed of d-variate polynomials of order at most $q \geq 1$ in each spatial variable. In our computations, we take $q := k + 1$, and we work with the Bezier–Bernstein basis
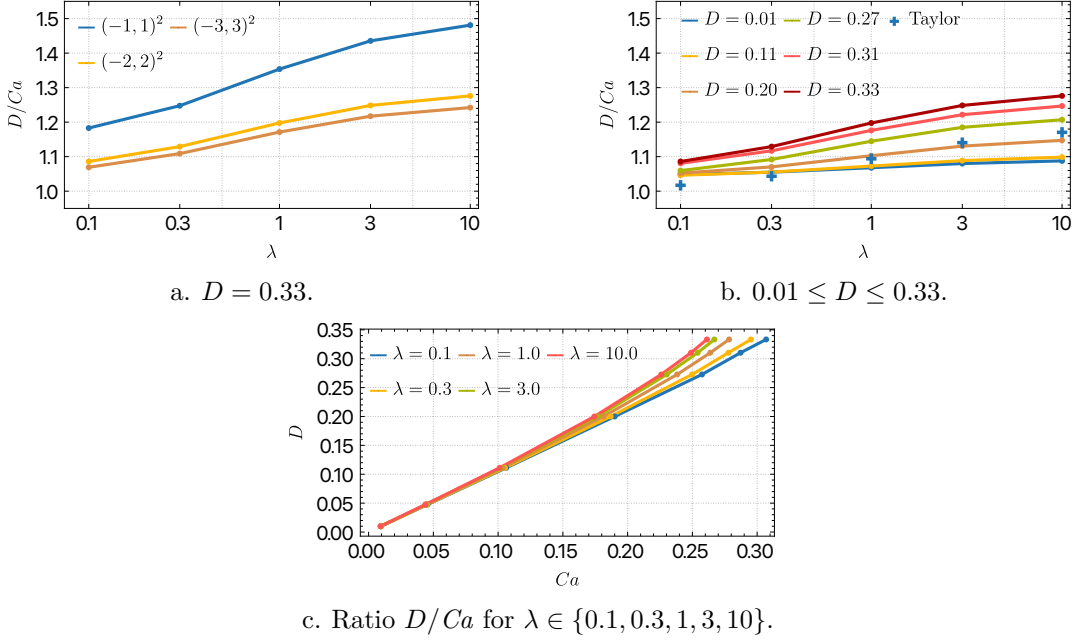
a. $D = 0.33$.

b. $0.01 \leq D \leq 0.33$.

c. Ratio D/Ca for $\lambda \in \{0.1, 0.3, 1, 3, 10\}$.

FIGURE 4.5. Figures 4.5.a and 4.5.b display the ratio D/Ca (Taylor deformation parameter over capillary number) as a function of the viscosity ratio λ. Figure 4.5.a: $D = 0.33$ and computational domains $(-a, a)^2$ with $a \in \{1, 2, 3\}$. Figure 4.5.b: $D \in \{0.01, 0.11, 0.20, 0.27, 0.31, 0.33\}$ and computational domain $(-2, 2)^2$; the blue crosses refer to the estimate from [38] derived under the assumption of small deformations. Figure 4.5.c displays D as a function of Ca; $\lambda \in \{0.1, 0.3, 1, 3, 10\}$ and computational domain $(-2, 2)^2$. We employ the unfitted HHO discretization with polynomial order $k = 1$.

functions, which present the advantage of taking values in $[0, 1]$ (see, e.g., [31, Chapter 2] and [4]). We define the initial discrete interface as

$$\Gamma_{\mathcal{T}}^0 := \{\boldsymbol{x} \in \Omega : \Phi_{\mathcal{T}}^0(\boldsymbol{x}) = 0\}, \tag{5.2}$$

where $\Phi_{\mathcal{T}}^0 := I_{\mathcal{T}}(\phi(t = 0, \cdot))$ is obtained with the Lagrange interpolation operator $I_{\mathcal{T}}$ onto $Q_q^{\mathrm{c}}(\mathcal{T})$.

At each iteration of the fixed-point scheme, we first solve, for a given interface, the velocity field (HHO solver, Section 3). Then we transport for some (fictitious) time the interface driven by the obtained velocity field. Specifically, at the iteration step $m \geq 0$ of the fixed-point scheme, the following two substeps are performed:

(1) Given the discrete interface $\Gamma_{\mathcal{T}}^m$ (kept fixed in this substep), we solve the HHO unfitted Stokes problem (2.1). Using the cell-agglomeration procedure from [9] produces a mesh $\mathcal{T}^m$ avoiding bad cuts (the superscript refers to $\Gamma_{\mathcal{T}}^m$), on which we seek approximations $\widehat{\boldsymbol{u}}_{\mathcal{T}}^m \in \widehat{\boldsymbol{U}}_{\mathcal{T}}^k$ and $\widehat{p}_{\mathcal{T}}^m \in P_{\mathcal{T}}^k$ of the velocity and pressure fields $(\boldsymbol{u}_i^m, p_i^m) \in H^1(\Omega_i; \mathbb{R}^d) \times L^2(\Omega_i)$, $i \in \{1, 2\}$, such that

$$-\nabla \cdot \boldsymbol{\sigma}_i^m = \boldsymbol{f}_i \qquad \text{in } \Omega_i^m, \quad i \in \{1, 2\}, \tag{5.3a}$$

$$\nabla \cdot \boldsymbol{u}_i^m = 0 \qquad \text{in } \Omega_i^m, \quad i \in \{1, 2\}, \tag{5.3b}$$

$$\boldsymbol{u}_2^m = \boldsymbol{g} \qquad \text{on } \partial\Omega, \tag{5.3c}$$

$$[\![\boldsymbol{u}^m]\!] = \boldsymbol{0}, \quad [\![\boldsymbol{\sigma}^m]\!]\boldsymbol{n}_{\Gamma}^m = \gamma H_{\Gamma}^m \boldsymbol{n}_{\Gamma}^m \quad \text{on } \Gamma_{\mathcal{T}}^m. \tag{5.3d}$$

More details on the calculation of the normal, $\boldsymbol{n}_\Gamma^m$, and the curvature, H_Γ^m, on the interface $\Gamma_{\mathcal{T}}^m$ are given in Section 5.2.

(2) Let $\triangle t^m = t^{m+1} - t^m$ be the fictitious time step such that the fixed-point iteration m is linked with the fictitious discrete time node $t^{m+1} := \sum_{j \in \{0:m\}} \triangle t^j$. We solve

$$\partial_t \widetilde{\Phi}_{\mathcal{T}}^m + \nabla \cdot \widetilde{\boldsymbol{f}}^m = 0 \qquad \text{in } \Omega \times (0, \triangle t^m), \tag{5.4a}$$

$$\widetilde{\Phi}_{\mathcal{T}}^m(\boldsymbol{x}, t) = \Phi_{\mathcal{T}}^0(\boldsymbol{x}) \qquad \text{on } \partial\Omega_{\text{in}} \times (0, \triangle t^m), \tag{5.4b}$$

$$\widetilde{\Phi}_{\mathcal{T}}^m(\boldsymbol{x}, 0) = \Phi_{\mathcal{T}}^m(\boldsymbol{x}) \qquad \text{in } \Omega, \tag{5.4c}$$

where

$$\widetilde{\boldsymbol{f}}^m(\boldsymbol{x}, t) := \boldsymbol{u}_{\mathcal{T}}^{m,c}(\boldsymbol{x}) \widetilde{\Phi}_{\mathcal{T}}^m(\boldsymbol{x}, t). \tag{5.5}$$

The inflow boundary $\partial\Omega_{\text{in}} := \{\boldsymbol{x} \in \partial\Omega : \boldsymbol{u}_{\mathcal{T}}^{m,c} \cdot \boldsymbol{n}_\Omega < 0\}$ is assumed to be independent of m (for simplicity). Moreover, $\boldsymbol{u}_{\mathcal{T}}^{m,c} \in Q_q^{\text{c}}(\mathcal{T}; \mathbb{R}^d)$ is a post-processed velocity field obtained by averaging at the interpolation nodes the values of the cell components of the HHO velocity field $\widehat{\boldsymbol{u}}_{\mathcal{T}}^m$ obtained in the first substep. The averaging is made using weights corresponding to the cell volumes. The problem (5.4) is solved numerically using continuous finite elements (of degree q) and a first-order graph viscosity ensuring a discrete maximum principle on the level-set function; we refer the reader to [22, 23, 24] for further insight. Finally, we update the level-set function by setting $\Phi_{\mathcal{T}}^{m+1} := \widetilde{\Phi}_{\mathcal{T}}^m(\triangle t^m)$ and evaluate $\Gamma_{\mathcal{T}}^{m+1}$ from $\Phi_{\mathcal{T}}^{m+1}$ by setting

$$\Gamma_{\mathcal{T}}^{m+1} := \left\{ \boldsymbol{x} \in \Omega : \Phi_{\mathcal{T}}^{m+1}(\boldsymbol{x}) = 0 \right\}. \tag{5.6}$$

Notice that the space discretization of (5.4) uses the original mesh $\mathcal{T}$ of Ω (without any agglomeration) and that we have $\widetilde{\Phi}_{\mathcal{T}}^m \in Q_q^{\text{c}}(\mathcal{T})$.

The above iterative scheme is stopped when the normal velocity at the interface is sufficiently small. It is not easy to give a quantitative tolerance a priori, but all the simulations reported in Section 6 achieve a reduction of the normal velocity at the interface by one to two orders of magnitude. A difficulty is that pushing the iterations too far generally results in some oscillations of the normal velocity, a phenomenon that can be attributed to the loss of mass and the resulting inaccuracy of the transport velocity when updating the interface.

Remark 5.1 (Fictitious time step). The time step used for the time discretization of the problem (5.4) is set to $dt^m := \triangle t^m / \widetilde{N}^m$, where $\widetilde{N}^m > 0$ is a prescribed value so that dt^m is small enough and

$$\triangle t^m \leq \min(c_1 \triangle t_\gamma, c_2 \triangle t_{\text{CFL}}^m). \tag{5.7}$$

Here, $\triangle t_\gamma := \frac{\mu_\sharp}{\gamma} h$ is considered to avoid that the interface moves too much during a fictitious time step. Moreover, $\triangle t_{\text{CFL}}^m$ results from the CFL condition ensuring a discrete maximum principle (see [22, 23, 24]). Finally, c_1, c_2 are user-dependent parameters. Hereafter, we set $\widetilde{N}^m \in [10, 100]$, $c_1 := 2$ and $c_2 := 0.05$, which typically leads to $dt^m \leq 10^{-2}$.

5.2. Normal and curvature for unknown interface

A well-known issue in problems driven by surface tension is the approximation of the normal and curvature on the interface. Indeed, although the level-set formulation has the advantage to provide analytic expressions for these quantities (see (2.7)), oscillations can appear (especially for the curvature) when discrete approximations of the level-set function are considered.

Let $\boldsymbol{n}_{\phi_{\mathcal{T}}^m}$ be the normal derived consistently with (2.7) from $\Phi_{\mathcal{T}}^m \in Q_q^{\mathrm{c}}(\mathcal{T})$, i.e.,

$$\boldsymbol{n}_{\phi_{\mathcal{T}}^m} = \frac{\nabla \Phi_{\mathcal{T}}^m}{\|\nabla \Phi_{\mathcal{T}}^m\|_{\ell^2}}. \tag{5.8}$$

At this stage, $\boldsymbol{n}_{\phi_{\mathcal{T}}^m}$ is a piecewise discontinuous field, so that its divergence is not well-defined; it can, however, be evaluated inside each mesh cell. A classical workaround is to smooth $\boldsymbol{n}_{\phi_{\mathcal{T}}^m}$ by using, for each component of $\nabla \Phi_{\mathcal{T}}^m$, the global L^2-orthogonal projection $\Pi_{\mathcal{T}}^q : L^2(\Omega) \to Q_q^{\mathrm{c}}(\mathcal{T})$ (a more local projection on patches can be considered to alleviate the costs). The resulting normal vector field being continuous and piecewise smooth, its divergence is well-defined. Unfortunately, setting

$$\begin{cases} \boldsymbol{n}_{\phi_{\mathcal{T}}^m}^{\mathrm{c}} := \dfrac{\Pi_{\mathcal{T}}^q(\nabla \Phi_{\mathcal{T}}^m)}{\|\Pi_{\mathcal{T}}^q(\nabla \Phi_{\mathcal{T}}^m)\|_{\ell^2}}, & H_{\phi_{\mathcal{T}}^m}^{\mathrm{c}} := -\nabla \cdot \boldsymbol{n}_{\phi_{\mathcal{T}}^m}^{\mathrm{c}}, \\ \boldsymbol{n}_{\Gamma}^{m,\mathrm{c}} := \boldsymbol{n}_{\phi_{\mathcal{T}}^m}^{\mathrm{c}}|_{\Gamma_{\mathcal{T}}^m}, & H_{\Gamma}^{m,\mathrm{c}} := H_{\phi_{\mathcal{T}}^m}^{\mathrm{c}}|_{\Gamma_{\mathcal{T}}^m}, \end{cases} \tag{5.9}$$

does not counter spurious oscillations. Additional smoothing is performed by means of a global L^2-orthogonal projection onto a suitable space of functions defined on the interface and that are continuous and piecewise polynomials. Recalling that the interface $\Gamma_{\mathcal{T}}^m$ is actually discretized by the parameters (l, n) (see (3.21)), we have

$$\Gamma_{\mathcal{T}}^m = \bigcup_{T \in \mathcal{T}^{\Gamma^m}} \bigcup_{j \in \{1:2^n\}} \Upsilon^{T,j}, \qquad \Upsilon^{T,j} := \boldsymbol{r}^{T,j}(\widehat{I}), \tag{5.10}$$

where $\widehat{I} := [0,1]$ and $\boldsymbol{r}^{T,j}$ is the geometric mapping defined by means of suitable interpolation nodes as in (3.20). Then, we introduce the space composed of continuous, piecewise polynomials of order $l' \in \{1:l\}$ over the interface, $P_{l'}^{\mathrm{c}}(\Gamma_{\mathcal{T}}^m)$, such that

$$P_{l'}^{\mathrm{c}}(\Gamma_{\mathcal{T}}^m) := \left\{ v \in \mathcal{C}^0(\Gamma_{\mathcal{T}}^m) : v_{|\Upsilon^{T,j}} \circ \boldsymbol{r}^{T,j} \in \mathbb{P}^{l'}(\widehat{I}), \ \forall T \in \mathcal{T}^{\Gamma^m}, \ \forall j \in \{1:2^n\} \right\}. \tag{5.11}$$

Let $\Pi_{l'}^{\Gamma} : L^2(\Gamma_{\mathcal{T}}^m) \to P_{l'}^{\mathrm{c}}(\Gamma_{\mathcal{T}}^m)$ be the L^2-orthogonal projection onto $P_{l'}^{\mathrm{c}}(\Gamma_{\mathcal{T}}^m)$. Then, we set

$$\boldsymbol{n}_{\Gamma}^{m,*} := \Pi_{l-1}^{\Gamma}(\boldsymbol{n}_{\Gamma}^{m,\mathrm{c}}), \qquad H_{\Gamma}^{m,*} := \Pi_1^{\Gamma}(H_{\Gamma}^{m,\mathrm{c}}), \tag{5.12}$$

where Π_{l-1}^{Γ} is applied component-wise for the normal vector. As above, more local projections on patches can be considered to alleviate the costs, although we observe that the projections in (5.12) are on a one-dimensional manifold, and are therefore relatively cheap. Notice also that, for the curvature, we always pick a piecewise affine representation to temper oscillations. Hereafter, we employ the definitions (5.12) to determine the normal and curvature on the interface.

6. Numerical results for unknown interface problems

In this section, we present our results for the equilibrium problem with unknown interface. First, we shortly discuss a couple of verification test cases. Then, we solve the equilibrium problem when the forcing flow at the far field is not of pure shear type. In all the figures presented in this section, the interface is obtained and plotted as a cloud of points which are all zeroes of the discrete level-set function $\Phi_{\mathcal{T}}^m$; we consider the $2^n l$ sampling points per mesh cell constructed as described in Section 3.3.

6.1. Verification test cases

In this section, we briefly present two verification test cases. Let us first consider an initial flower-like interface described by the level-set function

$$\phi^0(x, y) := x^2 + y^2 - R^2 + c \cos(m\theta), \tag{6.1}$$

with $\theta := \arctan\left(\frac{y}{x}\right)$ if $x \geq 0$, $\theta := \pi + \arctan\left(\frac{y}{x}\right)$ if $x < 0$, $R := 1/3$, $m := 4$ and $c := 0.04$. We set $\boldsymbol{f}_i := \boldsymbol{0}$, $\mu_i := 1$ (for $i \in \{1, 2\}$), $\boldsymbol{g} := \boldsymbol{0}$, and $\gamma := 1$, and there is no shear flow prescribed at the boundary. Hence, the interface is determined only by the surface tension force $\gamma H_\Gamma^{m,*} \boldsymbol{n}_\Gamma^{m,*}$, and the equilibrium shape is a circle. Since there is no shear flow prescribed at the boundary, we can consider a computational domain with a somewhat small size, namely $\Omega := (-0.5, 0.5)^2$.

a. Iteration $m = 20$, $t^m \approx 0.13$.

b. Iteration $m = 40$, $t^m \approx 0.33$.

c. Iteration $m = 80$, $t^m \approx 1.13$.
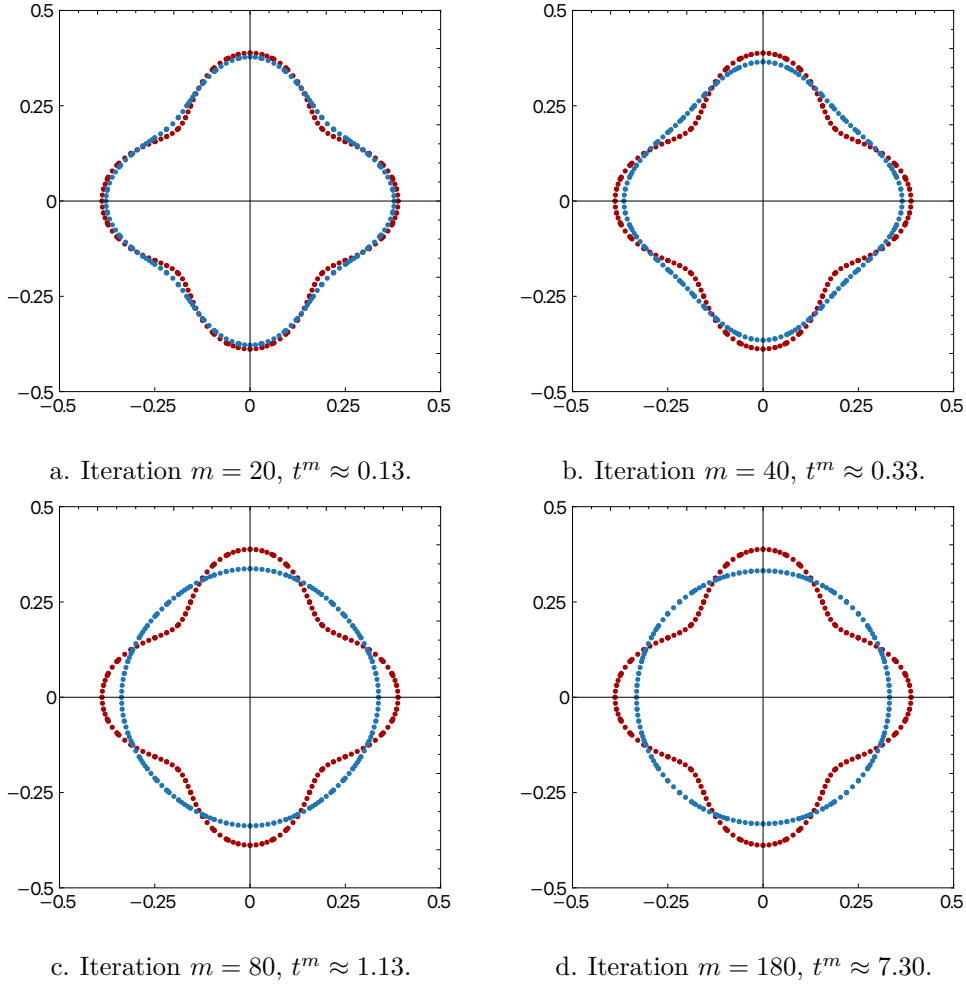
d. Iteration $m = 180$, $t^m \approx 7.30$.

FIGURE 6.1. First verification test case. In each panel, the red bullets represent the initial interface, and the blue ones the interface at iteration m of the fixed-point procedure. The HHO polynomial order is $k = 1$, and we employ $q = 2$ for the level-set approximation. The mesh is composed of 32×32 square cells. The interface discretization parameters are ($l = 2$, $n = 0$).

Starting from the flower-like interface, a few samples of the computed interface at some selected iterations of the fixed-point iterative procedure are illustrated in Figure 6.1. In this fashion, the time step is controlled by $\triangle t_{\mathrm{CFL}}^m$ for the first iterations, when the velocity field is strong owing to the high curvature produced by the flower-like interface, whereas the time step is controlled by $\triangle t_\gamma$ in the later iterations, when the velocity field is weaker so that larger time steps can be employed. Typical time steps are of the order of 10^{-3} for the first iterations and 10^{-1} for the later iterations.

Figure 6.2 displays some error indicators for various mesh-sizes (i.e., $h = 1/16, 1/32, 1/64$) as a function of the pseudo-time resulting from the fixed-point iterative scheme. We consider the curvature

and the normal velocity at the interface (measured either in the ℓ^∞- or L^1-norms, the former meaning that the maximum is computed by sampling over the nodes discretizing the interface), and the normalized error on the inner area Ω_1^m defined as

$$\text{diff}(A^m) := \frac{|\Omega_1^m| - |\Omega_1^0|}{|\Omega_1^0|}. \tag{6.2}$$

Notice that $\text{diff}(A^m)$ should vanish in the absence of discretization errors. This quantity is useful to study area loss, a phenomenon typical of the level-set approach. Reference quantities are calculated by using the fact that the circular equilibrium interface conserves the inner area of the initial interface. In all cases, the results reported in Figure 6.2 illustrate well how mesh refinement improves solution accuracy. We notice a somewhat unexpected result in Figure 6.2.d, where the coarsest mesh leads to a slightly better ℓ^∞-velocity error. We believe that this can be attributed to some compensation of errors, keeping in mind that all the errors are anyway very small (less than 10^{-7}). We also notice that this behavior is observed only in the special case where no shear flow is prescribed. In all the other cases studied in this section, mesh refinement always improves solution accuracy (see, e.g., Figure 6.6.d).

a. Error on inner area.

b. L^1-norm of normal velocity.

c. Curvature error at the interface.
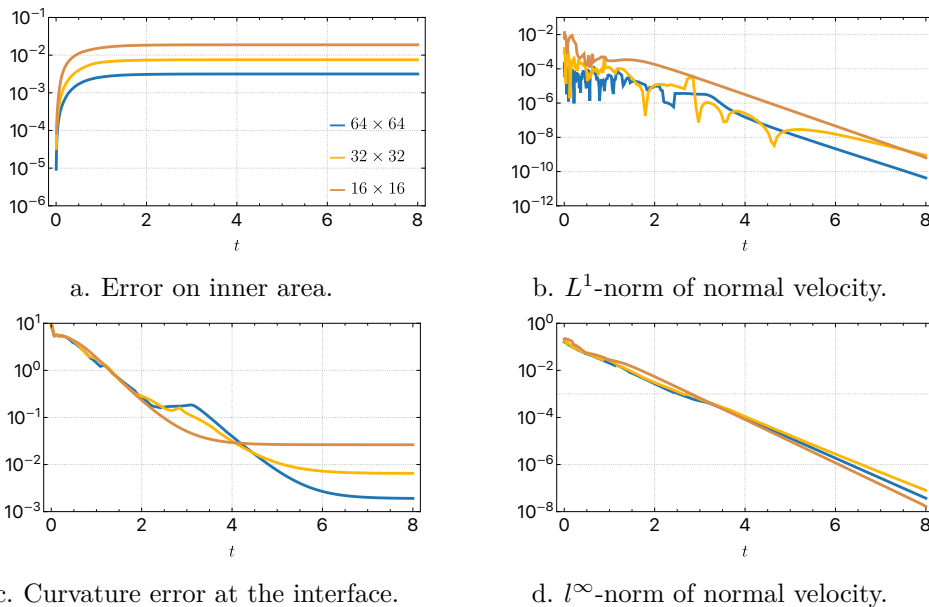
d. l^∞-norm of normal velocity.

FIGURE 6.2. First verification test case: error indicators. The HHO polynomial order is $k = 1$, and we employ $q = 2$ for the level-set approximation. The meshes are composed of 16×16 (brown line), 32×32 (yellow line), and 64×64 (blue line) square cells. The interface discretization parameters are ($l = 2$, $n = 0$). The number of fixed-point iterations is 100 for the case of the mesh composed of 16×16 square cells, and 180 for the case of meshes composed of 32×32 and 64×64 square cells.

In Figure 6.3, we show a few samples of the interface curvature at some selected iterations of the fixed-point iterative procedure. Since the equilibrium interface is circular, we expect that the curvature tends to a constant value equal to $H_* = -3$ (the reciprocal of the circle radius at equilibrium). Consistently, we find numerically that the curvature tends toward a constant value, that is slightly larger than the expected one owing to a slight loss of area.

In the second verification test case, we consider an initial circular interface described by the level-set function
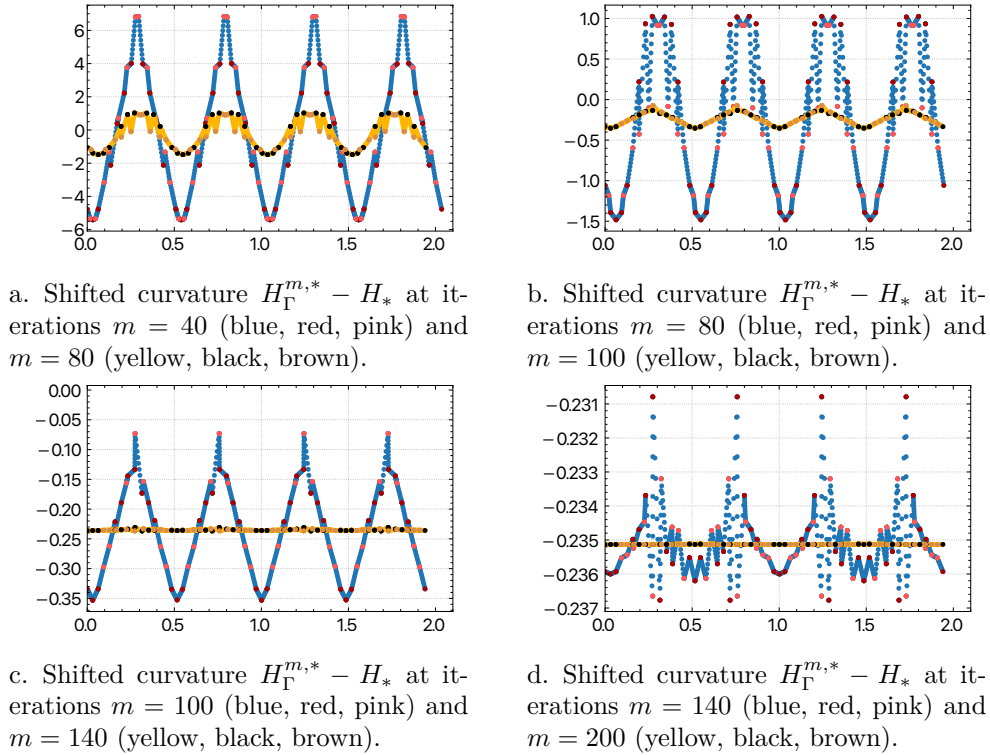
$$\phi^0(x, y) := x^2 + y^2 - R_*^2, \tag{6.3}$$

a. Shifted curvature $H_\Gamma^{m,*} - H_*$ at iterations $m = 40$ (blue, red, pink) and $m = 80$ (yellow, black, brown).

b. Shifted curvature $H_\Gamma^{m,*} - H_*$ at iterations $m = 80$ (blue, red, pink) and $m = 100$ (yellow, black, brown).

c. Shifted curvature $H_\Gamma^{m,*} - H_*$ at iterations $m = 100$ (blue, red, pink) and $m = 140$ (yellow, black, brown).

d. Shifted curvature $H_\Gamma^{m,*} - H_*$ at iterations $m = 140$ (blue, red, pink) and $m = 200$ (yellow, black, brown).

FIGURE 6.3. First verification test case. Shifted curvature $H_\Gamma^{m,*} - H_*$ (see (5.12)) as a function of the curvilinear abscissa along the interface at iteration $m \in \{40, 80, 100, 140, 200\}$ of the fixed-point procedure. For all the cut cells $T \in \mathcal{T}^{\Gamma^m}$, the blue (or yellow) bullets represent the values at the points inside T, the red (or black) bullets the values at the points on the boundary of T, and the pink (or brown) bullets the values at the points on the boundary of the agglomerated cells inside T. The HHO polynomial order is $k = 1$, and we employ $q = 2$ for the level-set approximation. The mesh is composed of 32×32 square cells. The interface discretization parameters are $(l = 2, n = 0)$.

with $R_* := 1/3$, and we set $\boldsymbol{f}_i := \boldsymbol{0}$, $\mu_i := 1$ (for $i \in \{1, 2\}$), and $\gamma := 1$. In contrast to the previous test case, we now consider the non-homogeneous Dirichlet boundary condition (4.1) enforcing a pure shear flow at the far field. The computational domain is set to $\Omega := (-1, 1)^2$. This size is a bit smaller than the size identified in Section 4 to achieve results independent of the size of the domain (namely, $\Omega := (-2, 2)^2$). The present size is chosen to reduce computational costs, keeping in mind that the numerical errors induced by the fixed-point iterative scheme and the geometric representation of the interface will dominate over the influence of the size of the domain (this has been verified numerically by comparing with some calculations on $\Omega = (-2, 2)^2$).

As above, we control the intensity of the shear by fixing the value of the capillary number to $Ca = \mu_2 \varepsilon L_* / \gamma$. Starting from the circular interface, the fixed-point iterative scheme described in Section 5.1 converges toward an elliptic equilibrium interface. We repeat the study for different values of the capillary number $Ca \in \{0.007, 0.07, 0.27\}$, corresponding to the values $\varepsilon \in \{0.01, 0.1, 0.4\}$. Some samples of the interface during the fixed-point scheme are illustrated in Figure 6.4 for $Ca = 0.27$.

Figure 6.5 reports some of the above error indicators for $Ca \in \{0.007, 0.07, 0.27\}$. In Figure 6.5.a, we observe that the convergence of the fixed-point procedure degrades when increasing the capillary number Ca. However, at a fixed capillary number Ca, convergence in space remains clearly visible in

Figure 6.6. In Figure 6.5.c, we report the normalized Taylor deformation parameter D/D_*. Here, D is estimated by assuming that the interface is always elliptic with axes parallel to the Cartesian axes (notice that the shear flow does not rotate the interface), and D_* corresponds to the value obtained using the steady calculations reported in Figure 4.5.c. The agreement is satisfactory owing to the geometric errors, with relative errors of the order of 20%.

a. Iteration $m = 200$, $t^m \approx 0.4$.   b. Iteration $m = 400$, $t^m \approx 0.8$.

c. Iteration $m = 600$, $t^m \approx 1.2$.   d. Iteration $m = 800$, $t^m \approx 1.6$.
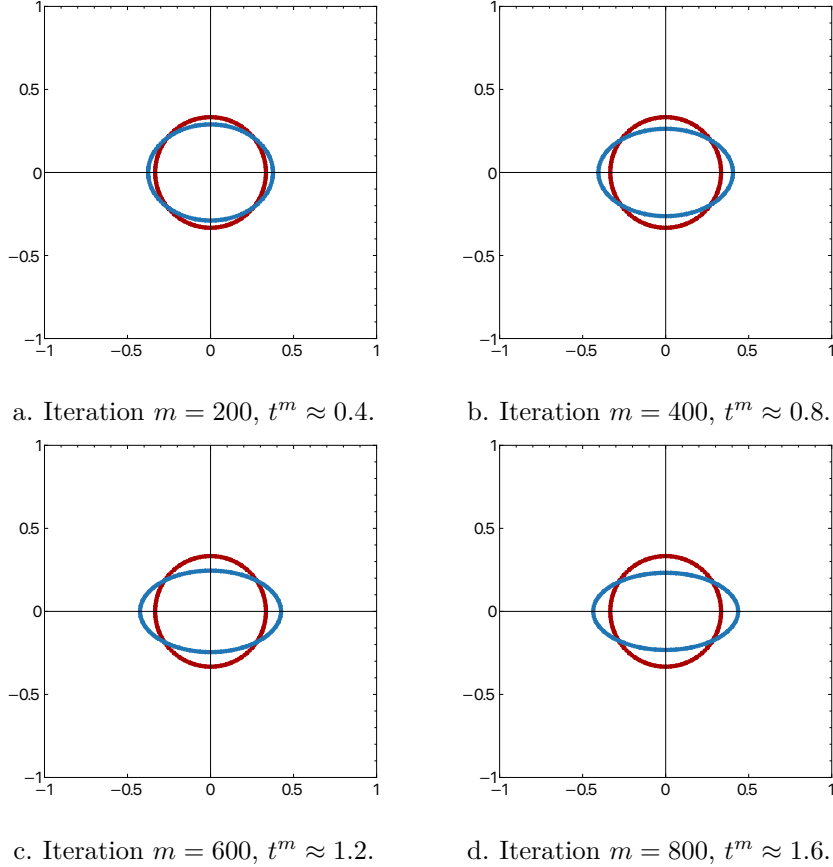
FIGURE 6.4. Second verification test case: $Ca = 0.27$ (i.e., $\varepsilon = 0.4$, $\gamma = 1$, $\mu_2 = 1$, $R_* = 1/3$). In each panel, the red bullets represent the initial interface, and the blue ones the interface at iteration m of the fixed-point procedure. The HHO polynomial order is $k = 1$, and we employ $q = 2$ for the level-set approximation. The mesh is composed of 64×64 square cells. The interface discretization parameters are ($l = 2$, $n = 0$).

a. Error on inner area.   b. l^∞-norm of normal velocity.   c. Ratio D/D_* (see caption)
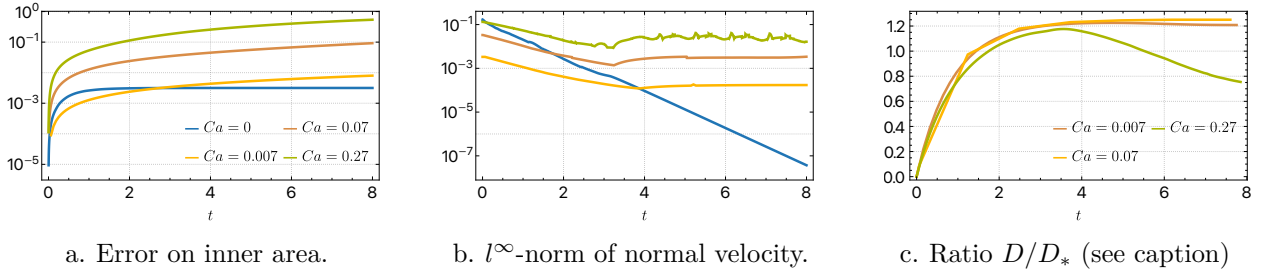
Figure 6.5. Second verification test case: error indicators (inner area, normal velocity at the interface, and Taylor deformation parameter) for $Ca \in \{0.007, 0.07, 0.27\}$ (i.e., $\varepsilon \in \{0.01, 0.1, 40\}$, $\gamma = 1$, $\mu_2 = 1$, $R_* = 1/3$), corresponding respectively to the yellow, brown, and green bullets. In Figures 6.5.a and 6.5.b, we additionally report the errors for $\varepsilon = 0$ (blue bullets). The HHO polynomial order is $k = 1$, and we employ $q = 2$ for the level-set approximation. The meshes are composed of 64×64 square cells. The interface discretization parameters are $(l = 2, n = 0)$. The number of fixed-point iterations is 210, 260, 1900, and 3900 for the cases $Ca = 0$, $Ca = 0.007$, $Ca = 0.07$, and $Ca = 0.27$, respectively.

a. Error on inner area.   b. L^1-norm of normal velocity.

c. Hausdorff distance $d(\Gamma_{\mathcal{T}}^{m+1}, \Gamma_{\mathcal{T}}^m)$ evaluated by sampling at the discrete nodes.   d. l^∞-norm of normal velocity.
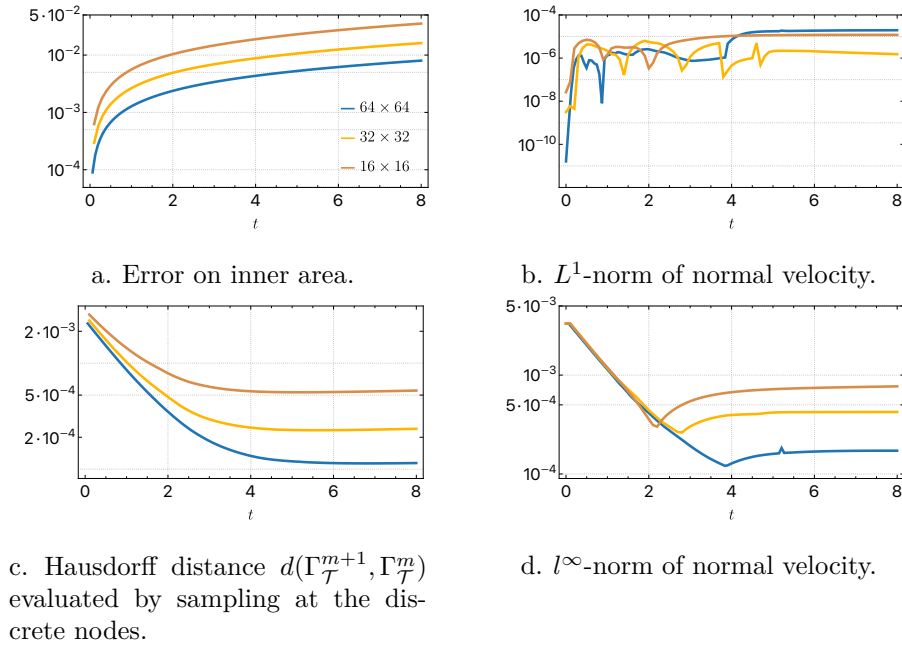
Figure 6.6. Second verification test case: error indicators for $Ca = 0.007$ (i.e., $\varepsilon = 0.01$, $\gamma = 1$, $\mu_2 = 1$, $R_* = 1/3$) for various levels of mesh refinement. The HHO polynomial order is $k = 1$, and we employ $q = 2$ for the level-set approximation. The meshes are composed of 16×16 (brown line), 32×32 (yellow line), and 64×64 (blue line) square cells. The interface discretization parameters are $(l = 2, n = 0)$. The number of fixed-point iterations is 21, 34, and 66 for 16×16, 32×32, and 64×64 square cells, respectively.

6.2. **Test cases with unknown interface**

Let us consider the initial circular interface described by the level-set function defined in (6.3) with $R_* := 1/3$, $\boldsymbol{f}_i := \boldsymbol{0}$, $\mu_i := 1$ for $i \in \{1,2\}$ (and thus the viscosity contrast is $\lambda = \mu_1/\mu_2 := 1$), and $\gamma := 1$. As in the previous section, we set $\Omega := (-1, 1)^2$. We now consider the following perturbation of the non-homogeneous Dirichlet boundary condition (4.1):

$$\boldsymbol{g} := \boldsymbol{u}_{\varepsilon|\partial\Omega}, \qquad \boldsymbol{u}_\varepsilon(x, y) := \varepsilon \left((x, -y)^{\mathrm{T}} + 0.5(\sin(\pi y), \sin(\pi x))^{\mathrm{T}} \right), \tag{6.4}$$

with $\varepsilon > 0$. We estimate the shear parameter as

$$\varepsilon_* = \max_{\boldsymbol{x} \in \Omega} \max_{i,j} |(\nabla^{\mathrm{s}} \boldsymbol{u}_\varepsilon)_{ij}(\boldsymbol{x})| = \varepsilon \frac{\pi}{2}, \tag{6.5}$$

so that the capillary number is now evaluated as follows:

$$Ca = \frac{1}{2} \mu \frac{\varepsilon \pi L_*}{\gamma}, \tag{6.6}$$

with $L_* := 2R_*$ and $\mu := \mu_1 = \mu_2$. In Figure 6.7.a, we illustrate the velocity field (6.4) without the interface (i.e., $\gamma = 0$), whereas in Figure 6.7.b, the presence of the interface is taken into account for the case $Ca = 0.27$ ($\varepsilon = 0.26$, $\gamma = 1$, $\mu_2 = 1$, $R_* = 1/3$). The interface evolution is illustrated in Figure 6.8 for the same value of the capillary number.
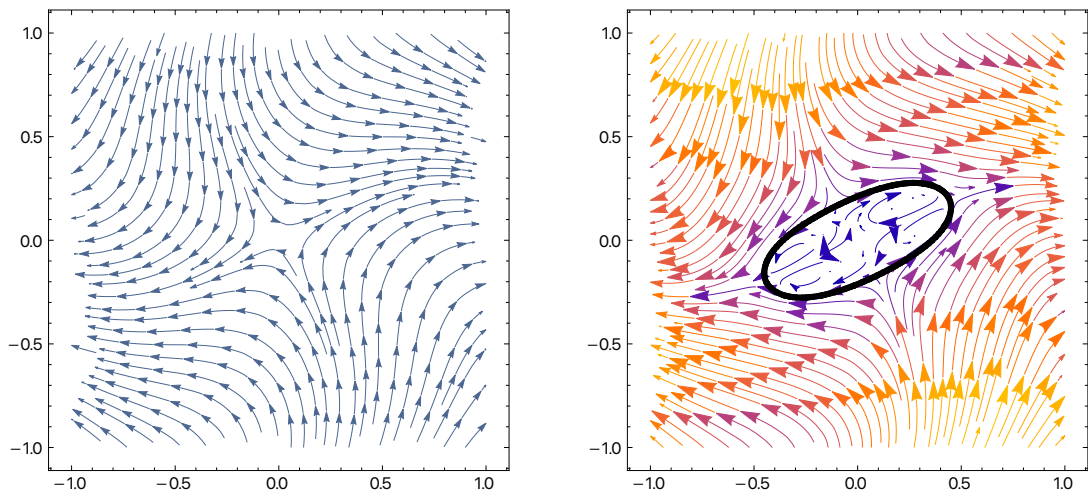
a. Streamlines for the perturbed velocity field (6.4).

b. Interface at iteration $m = 3000$, $t \approx 3$, for the perturbed shear flow with $Ca = 0.27$.

Figure 6.7. Streamlines for the test case with unknown interface. Figure 6.7.a illustrates the velocity field (6.4) without the interface (i.e., $\gamma = 0$), Figure 6.7.b includes the presence of the interface with $Ca = 0.27$ (i.e., $\varepsilon = 0.26$, $\gamma = 1$, $\mu_2 = 1$, $R_* = 1/3$). The HHO polynomial order is $k = 1$, and we employ $q = 2$ for the level-set approximation. The mesh is composed of 128×128 square cells. The interface discretization parameters are ($l = 2$, $n = 0$).

In Figure 6.9, we fix $\varepsilon = 0.26$ ($\gamma = 1$, $\mu_2 = 1$, $R_* = 1/3$) and we study the convergence in space of the fixed-point procedure. Consistently with the previous results on the verification test cases, the proposed methodology reduces the l^∞-norm of the normal velocity by a factor of 10. We notice that a more pronounced error reduction can be reached on finer meshes.

a. Iteration $m = 500$, $t^m \approx 0.5$.

b. Iteration $m = 1000$, $t^m \approx 1.0$.

c. Iteration $m = 3000$, $t^m \approx 3.0$.

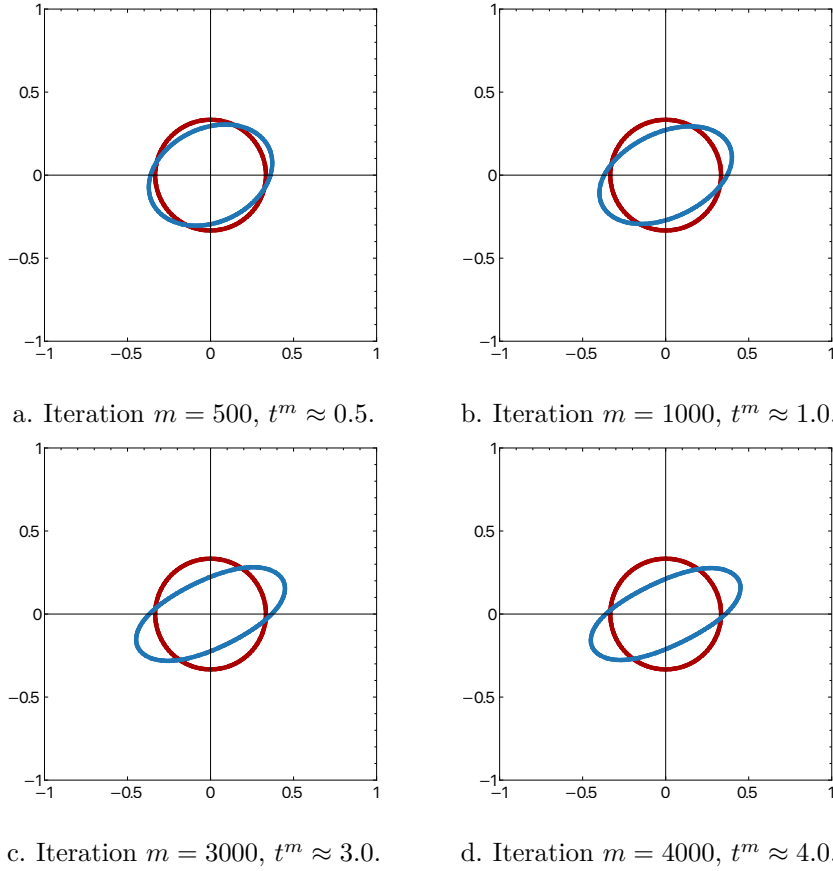d. Iteration $m = 4000$, $t^m \approx 4.0$.

FIGURE 6.8. Interface evolution for the test case with unknown interface with $Ca = 0.27$ (i.e., $\varepsilon = 0.26$, $\gamma = 1$, $\mu_2 = 1$, $R_* = 1/3$). In each panel, the red bullets represent the initial interface, and the blue ones the interface at iteration m of the fixed-point procedure. The HHO polynomial order is $k = 1$, and we employ $q = 2$ for the level-set approximation. The mesh is composed of 128×128 square cells. The interface discretization parameters are $(l = 2, n = 0)$.

6.3. Conclusions

The conclusion of the results on the verification test cases is that the convergence of the fixed-point procedure is in general satisfactory. However, some difficulties are encountered if one insists on reducing the normal velocity at the interface by more than an order of magnitude. This difficulty can possibly be alleviated by improving on the area loss, which, in turn, may be partly caused by the lack of divergence-free property of the post-processed velocity field used in substep 2 of the fixed-point iterative procedure. These points will be investigated in future work. Finally, in the case of an unknown interface, mesh refinement is again crucial to achieve a significant error reduction on the normal velocity, and thus approach a steady-state solution. Moreover, simulations become more challenging as the capillary number is increased. Indeed, higher curvatures contribute to the presence of sharp gradients, which demand finer spatial and temporal discretizations to accurately represent the associated flow patterns. It is also worth noting that as the capillary number is increased, the loss of area becomes more pronounced, inducing a larger error on the velocity approximation.

a. Error on inner area.

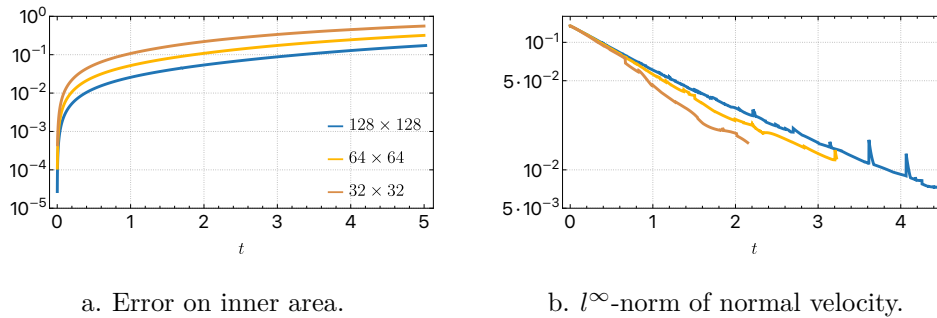b. l^∞-norm of normal velocity.

Figure 6.9. Error indicators for $Ca = 0.27$ (i.e., $\varepsilon = 0.26$, $\gamma = 1$, $\mu_2 = 1$, $R_* = 1/3$) for various levels of mesh refinement. The HHO polynomial order is $k = 1$, and we employ $q = 2$ for the level-set approximation. The meshes are composed of 32×32 (brown line), 64×64 (yellow line), and 128×128 (blue line) square cells. The interface discretization parameters are ($l = 2$, $n = 0$). The number of fixed-point iterations is 21, 2400, and 5100 for 32×32, 64×64, and 128×128 square cells, respectively.

References

[1] M. Abdelgawad and A. R. Wheeler. The Digital Revolution: A New Paradigm for Microfluidics. *Adv. Mater.*, 21(8):920–925, 2009.

[2] S. Adjerid, N. Chaabane, T. Lin, and P. Yue. An immersed discontinuous finite element method for the Stokes problem with a moving interface. *J. Comput. Appl. Math.*, 362:540–559, 2019.

[3] J. Aghili, S. Boyaval, and D. A. Di Pietro. Hybridization of mixed high-order methods on general meshes and application to the Stokes equations. *Comput. Methods Appl. Math.*, 15(2):111–134, 2015.

[4] M. Ainsworth. Pyramid algorithms for Bernstein-Bézier finite elements of high, nonuniform order in any dimension. *SIAM J. Sci. Comput.*, 36(2):A543–A569, 2014.

[5] R. Becker, E. Burman, and P. Hansbo. A Nitsche extended finite element method for incompressible elasticity with discontinuous modulus of elasticity. *Comput. Methods Appl. Mech. Eng.*, 198(41-44):3352–3360, 2009.

[6] E. Bezchlebová, V. Dolejší, and M. Feistauer. Discontinuous Galerkin method for the solution of a transport level-set problem. *Comput. Math. Appl.*, 72(3):455–480, 2016.

[7] L. Botti, D. A. Di Pietro, and J. Droniou. A hybrid high-order method for the incompressible Navier-Stokes equations based on Temam's device. *J. Comput. Phys.*, 376:786–816, 2019.

[8] J. U. Brackbill, D. B. Kothe, and C. Zemach. A continuum method for modeling surface tension. *J. Comput. Phys.*, 100(2):335–354, 1992.

[9] E. Burman, M. Cicuttin, G. Delay, and A. Ern. An unfitted hybrid high-order method with cell agglomeration for elliptic interface problems. *SIAM J. Sci. Comput.*, 43(2):A859–A882, 2021.

[10] E. Burman, G. Delay, and A. Ern. An unfitted hybrid high-order method for the Stokes interface problem. *IMA J. Numer. Anal.*, 41(4):2362–2387, 2021.

[11] E. Burman and A. Ern. An unfitted hybrid high-order method for elliptic interface problems. *SIAM J. Numer. Anal.*, 56(3):1525–1546, 2018.

[12] E. Cáceres, J. Guzmán, and M. Olshanskii. New stability estimates for an unfitted finite element method for two-phase Stokes problem. *SIAM J. Numer. Anal.*, 58(4):2165–2192, 2020.

[13] L. Cattaneo, L. Formaggia, G. F. Iori, A. Scotti, and P. Zunino. Stabilized extended finite elements for the approximation of saddle point problems with unfitted interfaces. *Calcolo*, 52(2):123–152, 2015.

[14] B. Cockburn, D. A. Di Pietro, and A. Ern. Bridging the hybrid high-order and hybridizable discontinuous Galerkin methods. *ESAIM, Math. Model. Numer. Anal.*, 50(3):635–650, 2016.

[15] R. G. Cox. The deformation of a drop in a general time-dependent fluid flow. *J. Fluid Mech.*, 37(3):601–623, 1969.

[16] D. A. Di Pietro and A. Ern. A hybrid high-order locking-free method for linear elasticity on general meshes. *Comput. Methods Appl. Mech. Eng.*, 283:1–21, 2015.

[17] D. A. Di Pietro, A. Ern, and S. Lemaire. An arbitrary-order and compact-stencil discretization of diffusion on general meshes based on local reconstruction operators. *Comput. Methods Appl. Math.*, 14(4):461–472, 2014.

[18] D. A. Di Pietro, A. Ern, A. Linke, and F. Schieweck. A discontinuous skeletal method for the viscosity-dependent Stokes problem. *Comput. Methods Appl. Mech. Eng.*, 306:175–195, 2016.

[19] A. Ern and J.-L. Guermond. *Finite Elements I: Approximation and Interpolation*, volume 72 of *Texts in Applied Mathematics*. Springer, 2021.

[20] C. Galusinski and P. Vigneaux. On stability condition for bifluid flows with surface tension: application to microfluidics. *J. Comput. Phys.*, 227(12):6140–6164, 2008.

[21] J. Gounley, G. Boedec, M. Jaeger, and M. Leonetti. Influence of surface viscosity on droplets in shear flow. *J. Fluid Mech.*, 791:464–494, 2016.

[22] J.-L. Guermond, M. Q. de Luna, and T. Thompson. A conservative anti-diffusion technique for the level set method. *J. Comput. Appl. Math.*, 321:448–468, 2017.

[23] J.-L. Guermond and M. Nazarov. A maximum-principle preserving C^0 finite element method for scalar conservation equations. *Comput. Methods Appl. Mech. Eng.*, 272:198–213, 2014.

[24] J.-L. Guermond and B. Popov. Invariant domains and first-order continuous finite element approximation for hyperbolic systems. *SIAM J. Numer. Anal.*, 54(4):2466–2489, 2016.

[25] A. Hansbo and P. Hansbo. An unfitted finite element method, based on Nitsche's method, for elliptic interface problems. *Comput. Methods Appl. Mech. Eng.*, 191(47-48):5537–5552, 2002.

[26] P. Hansbo, M. G. Larson, and S. Zahedi. A cut finite element method for a Stokes interface problem. *Appl. Numer. Math.*, 85:90–114, 2014.

[27] F. Heimann, C. Engwer, O. Ippisch, and P. Bastian. An unfitted interior penalty discontinuous Galerkin method for incompressible Navier-Stokes two-phase flow. *Int. J. Numer. Methods Fluids*, 71(3):269–293, 2013.

[28] A. Huebner, S. Sharma, M. Srisa-Art, F. Hollfelder, J. B. Edel, and A. J. deMello. Microdroplets: A sea of applications? *Lab Chip*, 8:1244–1254, 2008.

[29] H. Ji and Q. Zhang. A simple finite element method for Stokes flows with surface tension using unfitted meshes. *Internat. J. Numer. Methods Fluids*, 81(2):87–103, 2016.

[30] A. Johansson and M. G. Larson. A high order discontinuous Galerkin Nitsche method for elliptic problems with fictitious boundary. *Numer. Math.*, 123(4):607–628, 2013.

[31] M.-J. Lai and L. L. Schumaker. *Spline functions on triangulations*, volume 110 of *Encyclopedia of Mathematics and Its Applications*. Cambridge University Press, 2007.

[32] E. Olsson and G. Kreiss. A conservative level set method for two phase flow. *J. Comput. Phys.*, 210(1):225–246, 2005.

[33] E. Olsson, G. Kreiss, and S. Zahedi. A conservative level set method for two phase flow. II. *J. Comput. Phys.*, 225(1):785–807, 2007.

[34] S. Popinet. Numerical models of surface tension. volume 50 of *Annual Review of Fluid Mechanics*, pages 49–75. Annual Reviews, Palo Alto, CA, 2018.

[35] A. Reusken. Analysis of an extended pressure finite element space for two-phase incompressible flows. *Comput. Vis. Sci.*, 11(4-6):293–305, 2008.

[36] W. E. H. Sollie, O. Bokhove, and J. J. W. van der Vegt. Space-time discontinuous Galerkin finite element method for two-fluid flows. *J. Comput. Phys.*, 230(3):789–817, 2011.

[37] M. Sussman, A. S. Almgren, J. B. Bell, P. Colella, L. H. Howell, and M. L. Welcome. An adaptive level set approach for incompressible two-phase flows. *J. Comput. Phys.*, 148(1):81–124, 1999.

[38] G. I. Taylor. The formation of emulsions in definable fields of flow. *Proc. R. Soc. Lond., Ser. A*, 146(858):501–523, 1934.